Check for updates

Electron extraction layer-driven performance enhancement in CaHfSe₃ photovoltaics

Hicham El-assib,[a] Mohamed Alla,[ab] Safae Tourougui,[a]
Mustafa K. A. Mohammed, ![ORCID] *[cd] Shazia Akhtar Dar,[e] Yasmine Labghough,[f]
Malika Alla,[a] Naima,[g] Mustapha Rouchdi[a] and Boubker Fares[a]

Traditional solar cells – including those based on silicon or lead-halide perovskites – have a number of significant disadvantages, including long-term instability, costs, and toxicity. We demonstrate the suitability of CaHfSe₃ as a promising next-generation lead-free thermally stable absorber material. We performed a comprehensive numerical simulation study using SCAPS-1D to consider several device topologies of the type FTO/TiO₂ AZnO, WS₂/CaHfSe₃/MoO₃/Au, and to investigate the different features of a system based on CaHfSe₃. We conducted a full parametric study of the impacts of absorber thickness, defect density, acceptor doping and concentration, as well as carrier concentrations in the electron and hole transport layers. In addition, through experimentation we considered the operational characteristics of carrier generation-recombination methods, temperature and back contact effect current–voltage *I–V* characteristics, quantum efficiency, and the influence of series and shunt resistance. This allowed us to determine the optimized configuration. The top-performing structure, FTO/TiO₂/CaHfSe₃/MoO₃/Au, had an outstanding PCE of 32.39%, V_{OC} = 1.52 V, J_{SC} = 23.17 mA cm^{-2}, and FF = 91.41%. This research offers both fundamental insights and practical guidance for developing stable, efficient, and environmentally friendly CaHfSe₃-based solar cells. It paves the path for further experimental realization and commercial application.

1. Introduction

Transition to renewable energy sources has emerged as a global imperative to address the challenges posed by climate change and rising electricity demand. Among energy conversion technologies, solar cells have experienced significant growth thanks to advances in developing new semiconductor materials.[1,2] Although silicon-based photovoltaic cells currently dominate the market, they have certain limitations regarding manufacturing cost, efficiency, and stability. In particular, crystalline silicon suffers from intrinsic constraints as an indirect band gap semiconductor, its low absorption coefficient requires a minimum thickness to ensure sufficient light harvesting. Still, increasing thickness inevitably raises the series

[a](STCE)-Energy Research Centre (ERC), Faculty of Science, Mohammed V University, Rabat, Morocco

[b]MANAPSE Lab, Faculty of Sciences, Mohammed V University in Rabat, Morocco

[c]College of Remote Sensing and Geophysics, Al-Karkh University of Science, Baghdad 10011, Iraq. E-mail: dr.mustafa@ks.edu.iq

[d]College of Science, University of Warith Al-Anbiyaa, Karbala 56001, Iraq

[e]Department of Electronics and Communication Engineering, National Institute of Technology, Srinagar 190006, India

[f]Laboratory of Information Processing (LTI), Faculty of Sciences Ben MSick, University Hassan II, Casablanca, Morocco

[g]Department of Applied Physics, Delhi Technological Technology, Delhi 110042, India

resistance.[3] This trade-off between absorption and Joule losses fundamentally restricts the overall performance of silicon solar cells. These constraints have driven the exploration of alternative materials, especially perovskites, which are garnering increasing attention in this context due to their exceptional optical and electronic properties, cost-effectiveness, and sustainability for photovoltaic devices.[4–6] Specifically, MAPbX₃ or FABX₃ lead halide perovskites have demonstrated remarkable power conversion efficiency (PCE) of 27%.[7] However, conventional PSCs are weak in resilience to heat and humidity, have a high concentration of defects, are unstable due to the instability of organic cations, and contain poisonous lead (Pb), all of which pose significant health and environmental dangers, preventing their widespread commercialization. The primary obstacle is the search for lead (Pb)-free, stable, and eco-friendly materials. This is achieved by replacing cations such as Ge^{2+} or Sn^{2+}, which have advantageous band gaps, for Pb^{2+} ions.[8,9] However, the resultant perovskites are extremely unstable in air because of the strong oxidation propensity of Ge^{2+} and Sn^{2+} to Sn^{4+} and Ge^{4+}, respectively, which is linked to the increased energy levels of their respective 5s and 4s orbitals.[10] However, a major obstacle still stands in the way of these promising solar materials, poor durability.

This study is aimed at identifying materials with the positive attributes of lead halide perovskites while eliminating their

disadvantages. Chalcogenide perovskites are one of the most promising alternatives due to their non-toxic nature, impressive structural stability, and good electronic properties. These compounds typically adopt the ABX_3 structural formula, where A is an alkaline earth metal, B is a transition metal, and X is either sulfur (S) or selenium (Se).[11] A broad range of ABX_3 chalcogenide perovskites was recognized by Sun *et al.* in 2015 as potential absorber materials for solar applications. $BaZrS_3$, $CaZrS_3$, $SrZrS_3$, $BaHfS_3$, $CaHfS_3$, $SrHfS_3$, $CaTiS_3$, $BaZrSe_3$, $CaZrSe_3$, $SrZrSe_3$, $BaHfSe_3$, $SrHfSe_3$, and $CaTiSe_3$ are some of the more prominent instances.[12] Simulations highlight the strong potential of ABX_3-based solar cells, but experimental realization is limited by the complexity of film growth and ambient stability issues, as defects and exposure to moisture or oxygen can reduce efficiency. Overcoming these challenges is essential to achieve the predicted performance. Crystalline chalcogenide perovskite (CP) thin films are typically synthesized at high temperatures, greater than 600 °C (1170 F), severely limiting the ability to fabricate both single and multi-junction solar cells. The production of high-quality CP films *via* physical deposition methods or chemical sulfidation processes typically involves temperatures as high as 700 to 1000 °C (1292 to 1832 F), where intermediate products frequently include

impurity phases in the final composition.[13] Additionally, fabricating CP thin films *via* solution-based methods remains a significant challenge, as no known solvent can withstand the extreme temperatures needed for their synthesis. Furthermore, in 2025, Hayes *et al.* devised a comprehensive method for synthesizing various ABS_3 compounds, such as $BaZrS_3$, $BaTiS_3$, $SrZrS_3$, and $SrHfS_3$, together with colloidal phases synthesized within the Ba–Hf–S chemical system. These materials are composed of elements with a strong affinity for oxygen, notably group IV transition metals like Ti, Zr, and Hf.[14] This study identifies deficiencies in current research, noting that while $BaZrS_3$ nanoparticles have been manufactured in various phases by colloidal techniques, a consistent procedure for orthorhombic perovskite nanoparticles has not been established. To solve this, the authors introduce a high-temperature hot-injection technique, which allows precise control over the formation of colloidal $BaZrS_3$ nanoparticles, leading to a more reliable and scalable synthesis process. Recent studies on the ABS_3 chalcogenide perovskite show that replacing S with Se dramatically lowers the bandgap moving it away from the visible to the near-infrared wavelength. This transformation improves the capability for photovoltaic implementation and appear more favorable for transitioning solar energy technology.[15] Hf based perovskites still suffer from bulk recombination mainly due to Hf vacancy defects.[16] The lead-free perovskite $CaHfSe_3$ emerges as a viable alternative, as it combines the advantageous characteristics of semiconductors with properties comparable to its lead-based counterparts.
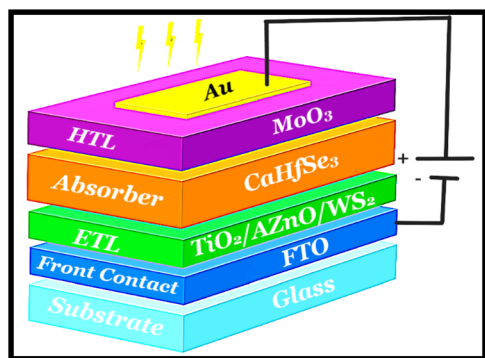

Fig. 1 The device architecture of the PSC based on $CaHfSe_3$.

Table 2 The contact work functions applied in the configurations

Metal contacts	Work function (eV) (ref. 8 and 18)
Cu	4.65
Fe	4.81
C	5
Au	5.1
Ni	5.5
Pt	5.7

Table 1 The key input values defining the architecture of the proposed solar cell

Parameters	FTO[18]	TiO$_2$ (ref. 16)	CaHfSe$_3$ (ref. 19)	WS$_2$ (ref. 20)	MoO$_3$ (ref. 21)	AZnO[8]
Thickness (μm)	0.1	0.03	Varied	0.03	0.03	0.03
Bandgap E_g (eV)	3.5	3.33	1.65	1.8	3.17	3.33
Electron affinity χ (eV)	4	4.55	4	3.95	2.05	4.55
Dielectric permittivity (relative)	9	8.12	7.93	13.6	12.5	8.12
N_c effective density of states in CB (cm^{-3})	2.2×10^{18}	4.1×10^{18}	8.9×10^{18}	1×10^{18}	2.21×10^{19}	4.1×10^{18}
N_v effective density of states in VB (cm^{-3})	1.8×10^{19}	8.2×10^{19}	1.1×10^{19}	2.4×10^{19}	1.8×10^{19}	8.2×10^{19}
$V_{th,e}$ velocity of electrons (cm s^{-1})	1×10^7	1×10^7	1×10^7	1×10^7	1×10^7	1×10^7
$V_{th,p}$ velocity of holes (cm s^{-1})	1×10^7	1×10^7	1×10^7	1×10^7	1×10^7	1×10^7
μ_n mobility of electrons (cm^2 V^{-1} s^{-1})	20	100	18.77	100	25	100
μ_p mobility of holes (cm^2 V^{-1} s^{-1})	10	20	6.81	100	100	20
N_D shallow uniform donor density (cm^{-3})	21×10^{19}	11×10^{13}	0	1×10^{18}	0	11×10^{13}
N_A shallow uniform acceptor density (cm^{-3})	0	0	1×10^{19}	0	1×10^{19}	0
N_t density of defect (cm^{-3})	1×10^{15}	1×10^{17}	1×10^{13}	1×10^{15}	1×10^{15}	1×10^{17}

These include favorable charge-carrier effective masses, a direct and optimal band gap, high absorption coefficients, and exceptional thermal stability, making it a promising absorber material for next-generation photovoltaics. The optical spectrum of the CaHfSe$_3$ reports a clear absorption edge which corresponds to a direct electronic bandgap of 1.65 eV.[15] This optimization study of CaHfSe$_3$-based perovskite solar cells (PSCs) focuses on various combinations of electron and hole transport layers (ETL–HTL), using SCAPS-1D simulations, a one-dimensional solar cell modelling software based on capacitance. To enhance device performance, MoO$_3$ is employed as the HTL in combination with TiO$_2$, WS$_2$, and AZnO as ETL candidates. Key operational parameters such as back contact material, series resistance, and operating temperature are systematically examined. Additionally, the effects of absorber layer thickness and doping concentration are optimized to further improve cell efficiency. Analysis of current–voltage (J–V) characteristics and external quantum efficiency (EQE) confirms that the optimized configuration yields a significantly enhanced power conversion efficiency (PCE) compared to previously reported designs.

2. Device architecture and computational methodology

2.1. Numerical modeling technique

The numerical method employed in this research is based on simulations conducted with SCAPS-1D 3.3.11 (Solar Cell Capacitance Simulator – 1D), a widely used software for modeling the electrical behavior of thin-film solar cells, which solves the coupled Poisson's and continuity equations under steady-state conditions. As shown in eqn (1) Poisson equation, relates electrostatic potential to charge density in the material within the device:[17]

$$\frac{d^2\psi}{dx^2} = \frac{-q}{\varepsilon}[p(x) - n(x) + N_D^+(x) - N_A^-(x) + p_t(x) - n_t(x)] \quad (1)$$

With ε: dielectric constant, q: electron charge, ψ: electrostatic potential, n, and p: free electrons and holes, n_t and n_p: trapped electrons and holes, N_D^+ and N_A^-: represent the densities of ionized donors and acceptors, respectively.

Poisson's equation must be solved in order to analyze solar cells since it shows how the electric potential is dispersed
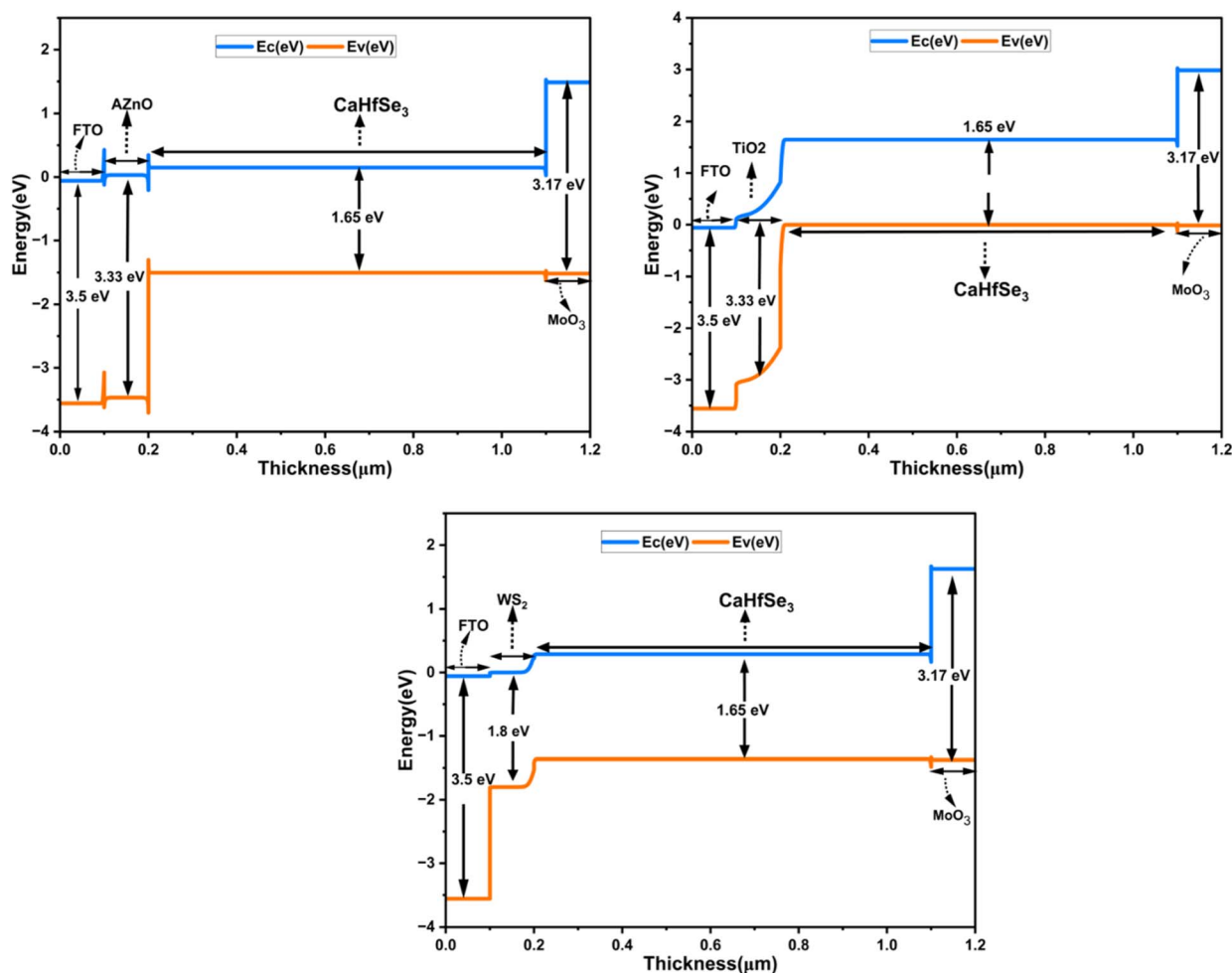

Fig. 2 CaHfSe$_3$-based PSC energy diagram with MoO$_3$ as the HTL and (a) AZnO, (b) TiO$_2$, and (c) WS$_2$ as the ETL.
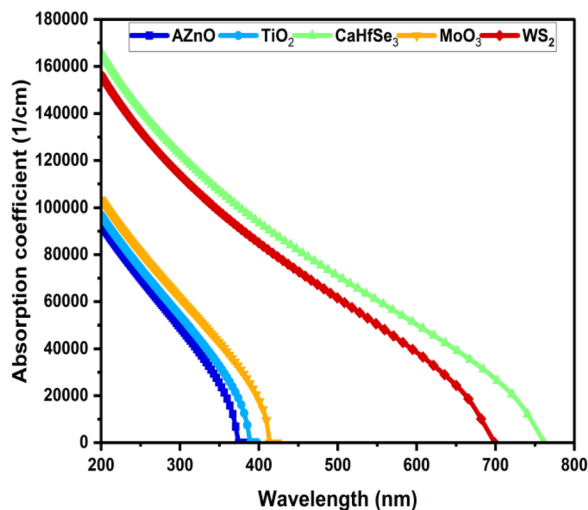
Fig. 3 Absorption coefficients of $CaHfSe_3$, TiO_2, AZnO, WS_2, and MoO_3 as a function of wavelength.

throughout the device's many layers. This knowledge facilitates the analysis of charge carrier dynamics, which involves the movement and recombination of electrons and holes to generate energy. The continuity equations reflect the principle of charge conservation and describe the motion of charge carriers in semiconductors. In this case, eqn (2) and (3) represent continuity equations for electrons and holes, respectively.

$$\frac{dp}{dt} = \frac{1}{q}\frac{dJ_p}{dx} + R_p(x) - G(x) \tag{2}$$

$$\frac{dn}{dt} = \frac{1}{q}\frac{dJ_n}{dx} + R_n(x) - G(x) \tag{3}$$

where G is the photogeneration rate, R_n and R_p are the rates of recombination of electrons and holes, respectively and J_n and J_p being the electrical current densities of electrons and holes. In semiconductor materials, electrons or holes can be migrating for two reasons—there is an electric field that produces a drift
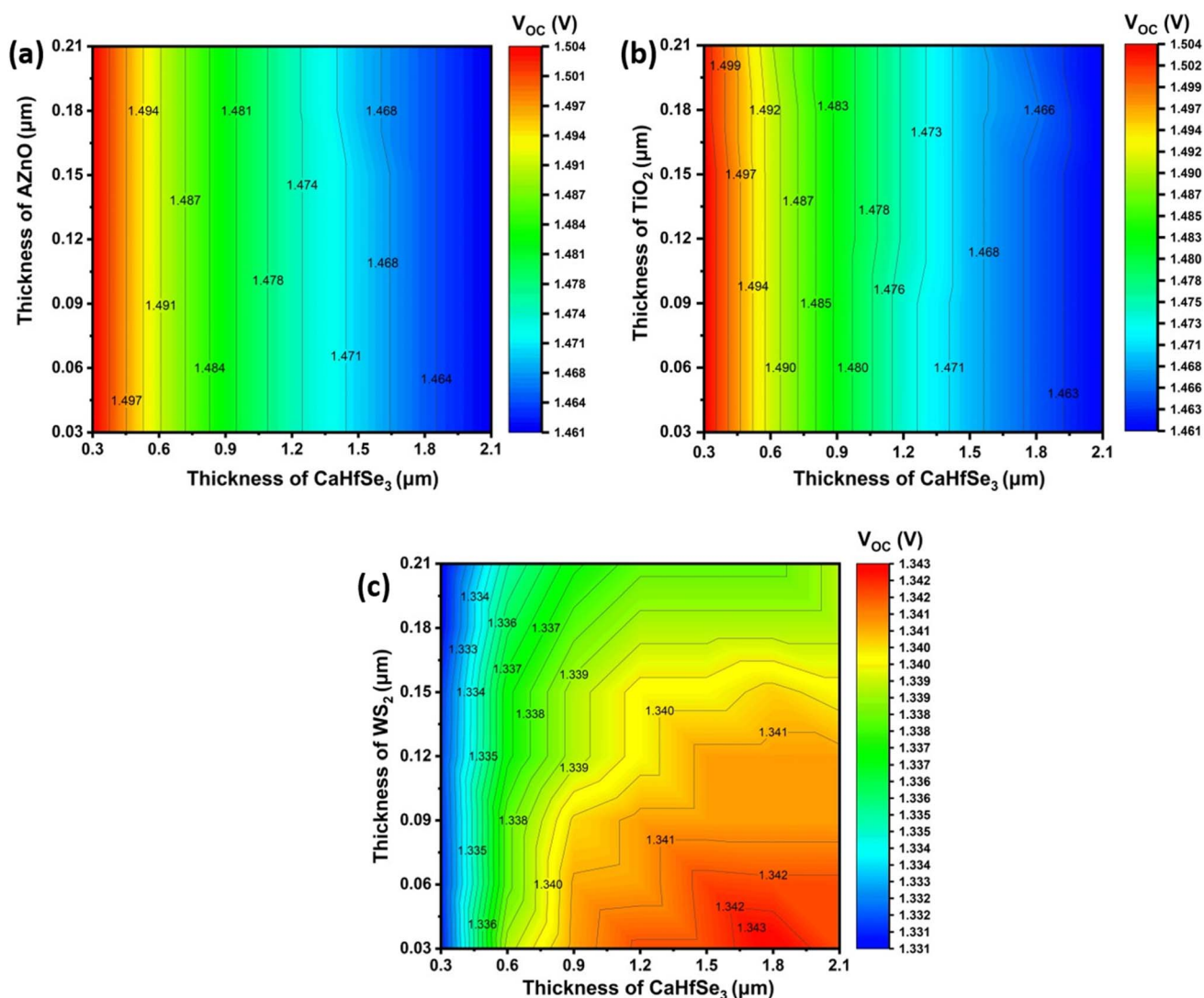

Fig. 4 V_{OC} contour mapping for (a) AZnO, (b) TiO_2, and (c) WS_2 ETLs with $CaHfSe_3$ absorber thickness.

current or there is a concentration gradient of carriers so that there is a diffusion current. Eqn (4) and (5) describe the electrical current densities associated with electron and hole transport.

$$J_n(x) = qD_n \frac{\partial n}{\partial x} + q\mu_n(n)\frac{\partial \varnothing}{\partial x} \tag{4}$$

$$J_p(x) = qD_p \frac{\partial p}{\partial x} + q\mu_p(p)\frac{\partial \varnothing}{\partial x} \tag{5}$$

Using the optical absorption model, the optical absorption constant α is computed, as shown in eqn (6).

$$\alpha(\lambda) = \left(A + \frac{B}{h\upsilon}\right)\sqrt{h\upsilon - E_g} \tag{6}$$

where υ is the radiation frequency, E_g is the material's real band gap, h is Planck's constant, and A and B are the model parameters.

2.2. Simulation settings and device structure

In the current work, SCAPS-1D Software was used to model a device with the structure of (back metals/MoO$_3$/CaHfSe$_3$/ETMs/FTO), as shown generally in Fig. 1, to simulate the one-dimensional performance of a thin films photovoltaic device. The ETMs WS$_2$, AZnO, and TiO$_2$ were used due to their properties that complement the structural and electronic fabric of the ETLs for improved extraction of electrons through the layers to the collecting circuits of solar cell architectures. The two different ETLs are used along with MoO$_3$ as a hole transport layer or HTL layer and the studies explored the pairs of combinations that produced the best configuration for the device. The materials used for the CaHfSe$_3$ absorber layer, the FTO-coated glasses, which are transparent conducting materials, and the back contact varied with Cu, Fe, Au, C, Ni, and Pt. The project is focused on improving the metrics and performance of CaHfSe$_3$-based lead-free perovskite solar cells by simulating modifications to the HTLs (WS$_2$, AZnO, TiO$_2$), and ETL(MoO$_3$), and the back contacts (Cu, Fe, Au, C, Ni, Pt). For
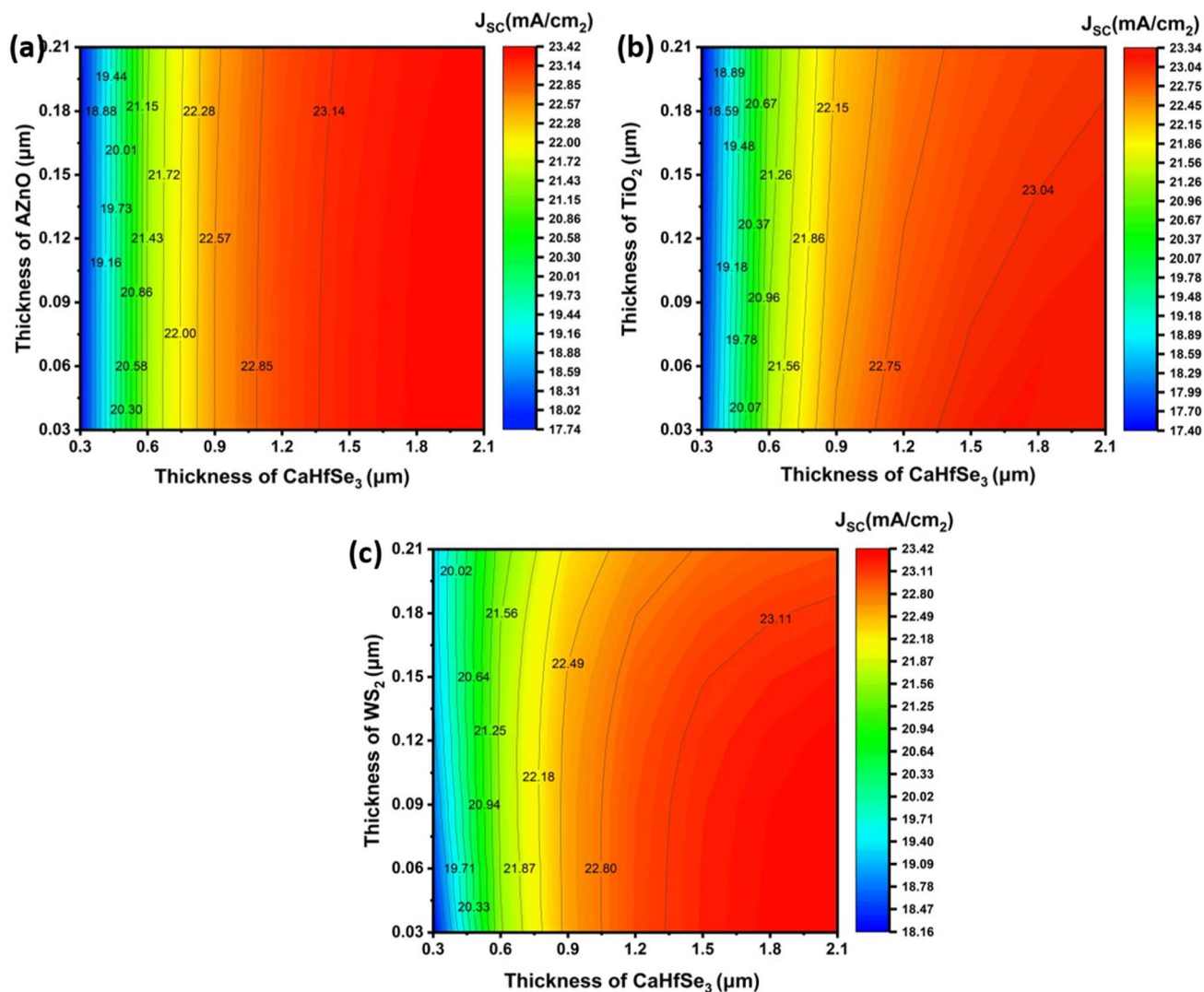

Fig. 5 J_{SC} contour mapping for (a) AZnO, (b) TiO$_2$, and (c) WS$_2$ electron transport layers (ETLs) as a function of CaHfSe$_3$ absorber thickness.

each layer, key parameters were defined, such as thickness, bandgap energy, electron affinity, permittivity, doping concentration, carrier mobilities, and defect densities, are listed in Table 1.

Table 2 presents the work functions of various materials, including Gold (Au), Nickel (Ni), Carbon (C), Iron (Fe), Copper (Cu), and Platinum (Pt). The simulations were conducted under standard AM1.5G illumination (1000 W m^{-2}) at an operating temperature of 300 K. Additionally, series/shunt resistances and working temperature were incorporated to reflect realistic electrical behavior. Device performance was assessed using J–V characteristics, quantum efficiency (QE), and power conversion efficiency (PCE), with systematic variation of key parameters to determine the optimal configuration.

3. Outcome analysis and interpretation

3.1. The band diagram of the model cell

Simulated band diagrams for the proposed structures are shown in Fig. 2, highlighting the importance of energy level alignment in achieving efficient charge separation and high photovoltaic performance. To ensure effective electron transport, the electron affinity of the electron transport layer (ETLs) must exceed that of the CaHfSe$_3$ absorber, facilitating downward conduction band alignment.[22] Conversely, hole extraction is enhanced when the ionization potential of the hole transport layer (MoO$_3$) is lower than that of the absorber, ensuring a smooth flow of holes.[23]

The WS$_2$/CaHfSe$_3$ interface exhibits a small CBO (0.02 eV), indicating good energy level continuity and promoting efficient electron transport. In the case of TiO$_2$, which has a wide E_g of 3.33 eV, the conduction band alignment (0.01 eV) also supports efficient electron extraction while acting as a barrier to hole backflow. The AZnO/CaHfSe$_3$ interface shows a conduction band offset of approximately 0.03 eV, reflecting strong energetic compatibility and potential for high electron collection efficiency. On the hole transport side, the CaHfSe$_3$/MoO$_3$ interface demonstrates a favorable valence band offset (VBO), as the valence band maximum (VBM) of MoO$_3$ lies below that of CaHfSe$_3$. This ensures selective and efficient hole extraction while suppressing electron recombination at the back contact.

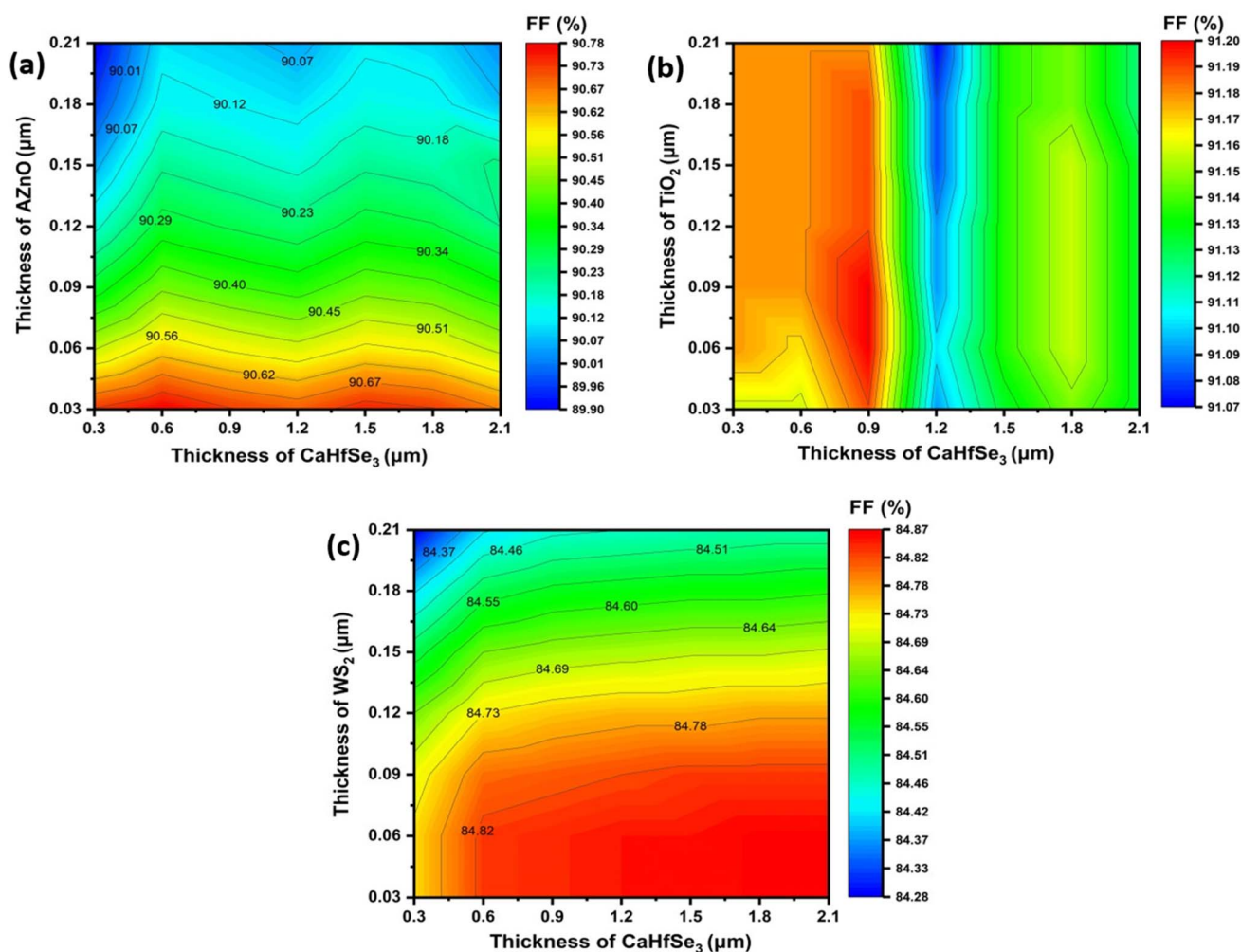Fig. 6 Contour mapping of the fill factor (FF %) for different ETL materials: (a) AZnO, (b) TiO$_2$, and (c) WS$_2$.

Altogether, these band alignments confirm the suitability of WS_2, TiO_2, and AZnO as ETLs, and MoO_3 as an HTL, in facilitating efficient charge separation and transport in $CaHfSe_3$-based photovoltaic devices.

3.2. Coefficient of absorption

The coefficient of absorption (α) as a function of wavelength indicates a material's ability to absorb light across various regions of the electromagnetic spectrum (UV, visible, and infrared). Fig. 3 displays the theoretical absorption profiles for all layers. The absorbent material $CaHfSe_3$ is notable for its strong Capability of absorbing radiation in the visible region, with values exceeding 10^5 cm^{-1} between 400 and 770 nm. This characteristic makes it an excellent choice for harnessing solar light and producing charge carriers. TiO_2 and AZnO, used as electron transport layers (ETL), exhibit very low absorption coefficients (less than 10^2 cm^{-1} between 350 nm and 700 nm), allowing light to pass through with minimal absorption and facilitating optimal transmission to the active $CaHfSe_3$ layer. Finally, MoO_3, used as a hole transport layer (HTL),

demonstrates intermediate behavior with a low absorption coefficient (around 10^3) in the 350–700 nm range, minimizing interaction with incident light. Its absorption increases slightly in the UV range but remains compatible with its role.[24]

3.3. Impact of ETL and absorber thickness on device performance

To improve light harvesting and promote efficient extraction of charge carriers, the absorption and ETL thicknesses must be carefully chosen and optimized. Maximum photon absorption in the active layer and efficient electron transport are ensured by a well-optimized design. In this study, contour plots were used to investigate the impact of absorber and ETL thickness variations on the performance of $CaHfSe_3$ architectural performance has been investigated. Through this research, we can investigate how altering the thickness of the absorber and electron transport layers affects key performance metrics, including V_{OC}, FF, J_{SC}, and PCE. To identify the optimal thickness combinations for enhanced device performance, the contour plots display the predicted values of J_{SC}, V_{OC}, FF, and PCE across

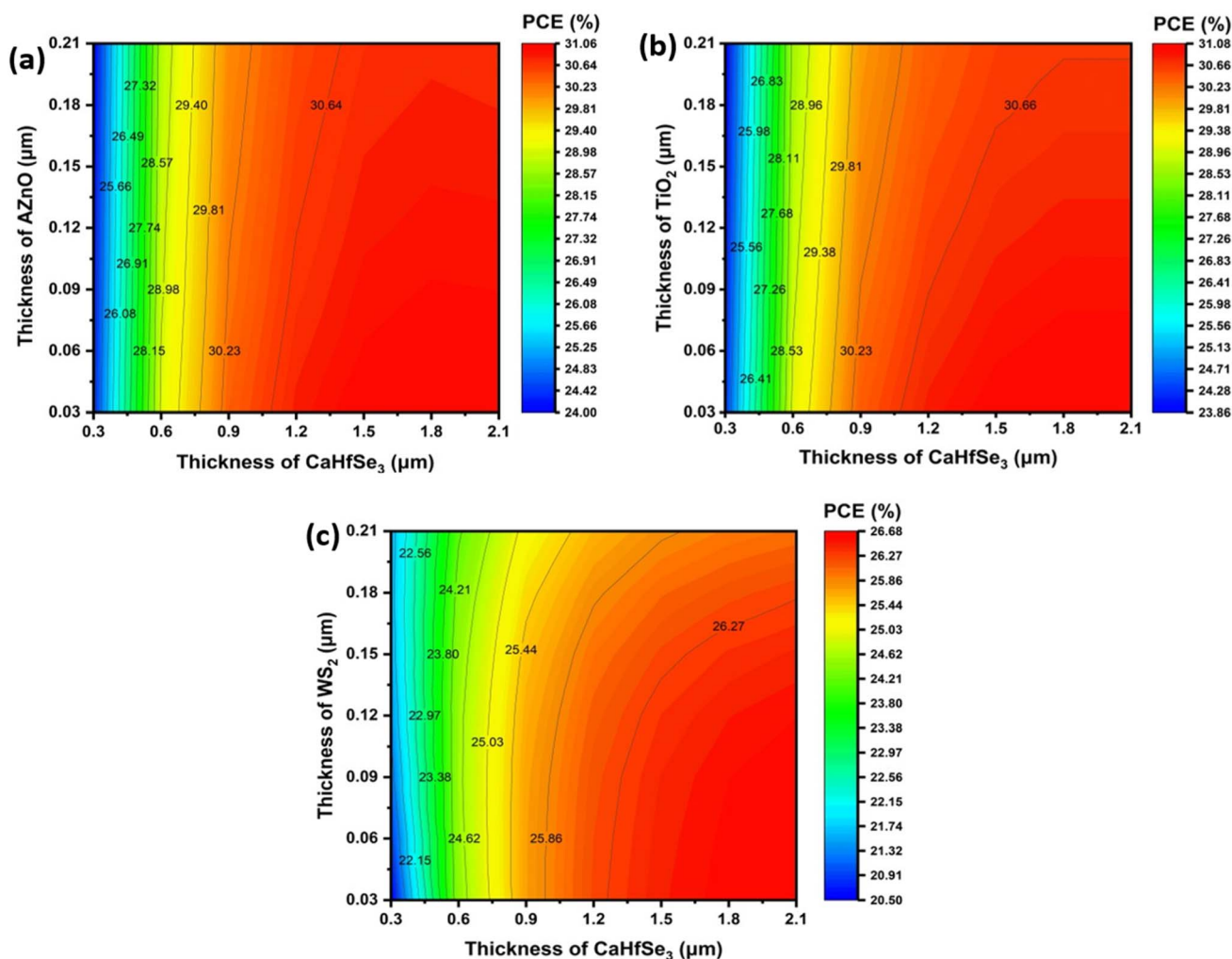**Fig. 7** Contour mapping of PCE (%) when ETL is (a) AZnO, (b) TiO_2, and (c) WS2.

a range of absorber thicknesses (300 to 2100 nm) and ETL thicknesses (from 30 to 210 nm). In this investigation section, MoO$_3$ was held constant as the HTM. Fig. 4 shows the impact of absorber layer thickness and ETL on the V_{OC}. Under conditions where the absorber and ETL layers were about 300 nm and <150 nm in thickness, respectively, the perovskite employing TiO$_2$ and AZnO as ETLs reached a peak V_{OC} of 1.54 V, as illustrated in Fig. 4(a and b). As the thicknesses of both the absorber and ETL layers grew, the open-circuit voltage (V_{OC}) exhibited a decline. This decrease can be attributed to a rise in the reverse saturation current caused by the thicker absorber, combined with the partial absorption of incident light within the thicker ETL layers. By contrast, when absorber and ETL thicknesses were approximately 1500 nm and ≤30 nm, respectively, the PSC with a WS$_2$ ETL showed a maximum V_{OC} of 1.34 V.

The influence of changes in the absorber layer thickness and ETL on the J_{SC} parameter of three selected perovskite solar cells is illustrated in Fig. 5. The PSC incorporating TiO$_2$ as the ETL achieved a maximum current density of 23.33 mA cm^{-2} once the absorber layer exceeded 1800 nm and the ETL thickness was

≥30 nm. Under conditions where the absorber measured 2100 nm and the thickness of ETL ranged from 30 to 210 nm, the ETL AZnO demonstrated the greatest J_{SC} of 23.4 mA cm^{-2}. In addition, the PSCs using WS2 ETL exhibited maximum (J_{SC}) of 23.4 mA cm^{-2} when the absorber thickness was 2100 nm and the ETL thickness ranged from 30 to 90 nm. Generally, an increase in absorber thickness led to higher J_{SC} values in each device, as a thicker absorber enhances photon absorption, promotes greater electron–hole pair generation, and consequently boosts the photocurrent. This enhancement is also ascribed to the improved spectral responsiveness at extended wavelengths. Fig. 6 illustrates how different absorber and ETL layer thicknesses affect FF values. When WS$_2$ is implemented as the electron transport layer (ETL) in solar cell structures, studies have revealed that the FF of BaHfSe$_3$-based solar cells increase with absorber thickness up to 1.8–2.1 μm, while it slightly decreases as the WS$_2$ layer becomes thicker. The highest FF value of 84.86% is recorded when the BaHfSe$_3$ thickness ranges from 1.8 to 2.1 μm and the WS$_2$ thickness is between 0.03 and 0.06 μm, Fig. 6(b).
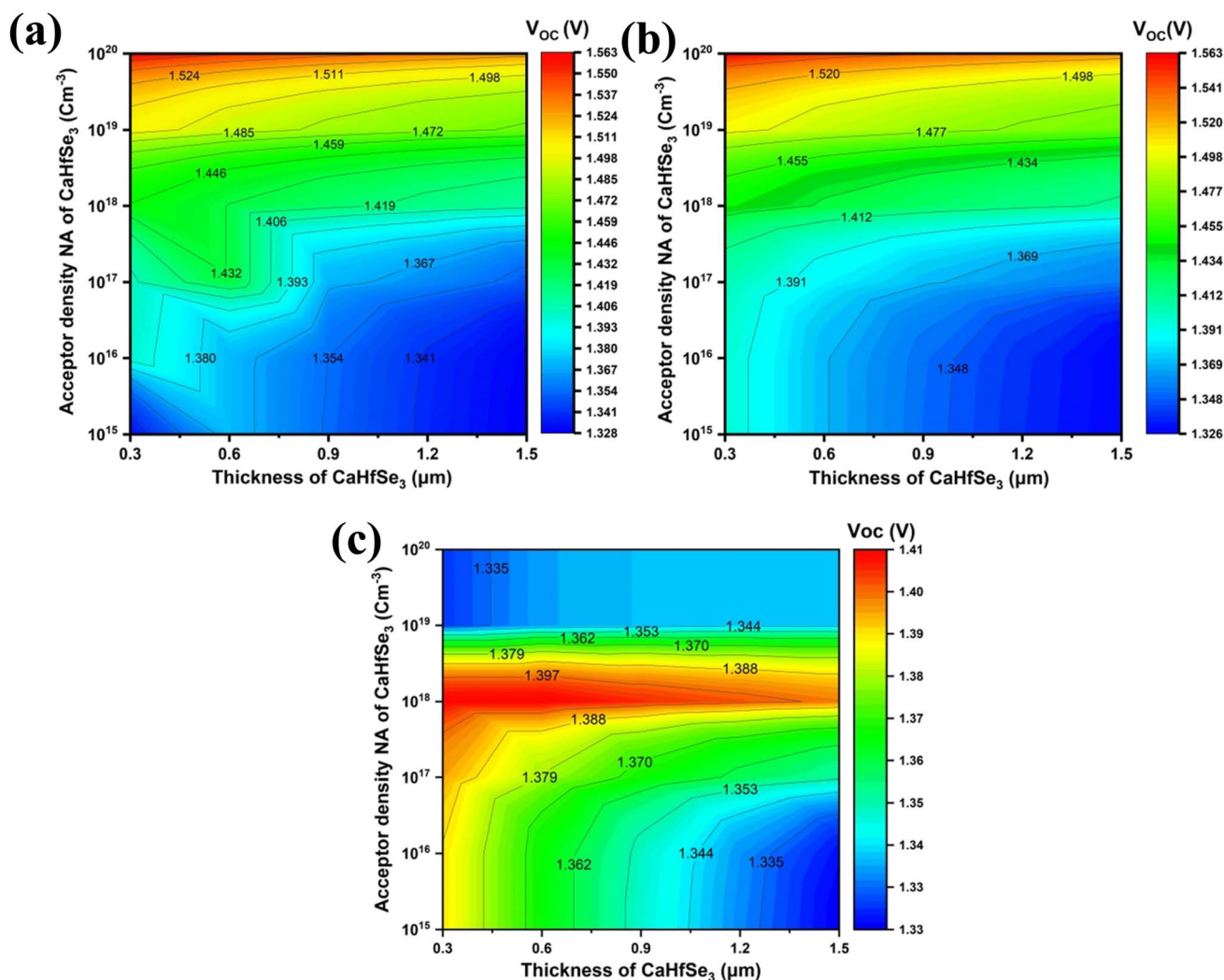

Fig. 8 Contour plots illustrate the influence of absorber doping concentration and thickness on V_{OC} for ETL types (a) AZnO, (b) TiO$_2$, and (c) WS$_2$.

Using TiO$_2$ as an ETL results in a maximum fill factor (FF) of 91.2% with a BaHfSe$_3$ thickness of 0.9 μm and a TiO$_2$ layer thickness ranging from 0.06 to 0.09 μm. In contrast, increasing the thickness of BaHfSe$_3$ beyond 1.2 μm leads to a slight decline in FF, likely resulting from enhanced recombination losses or reduced efficiency in charge transport. Furthermore, Fig. 6(a) illustrates that the AZnO electron transport layer thickness significantly impacts the fill factor (FF), with ultrathin layers (≤0.03 μm) showing optimal values (~90.7%). FF gradually decreases as AZnO thickness increases, primarily due to heightened recombination losses and series resistance. Conversely, variations in the BaHfSe$_3$ absorber's thickness have minimal effect on the FF, indicating consistent device performance over a wide thickness range (0.3–2.1 μm), as charge carrier extraction and production remain unchanged. Fig. 7 displays the simulation findings showing distinct performance characteristics for the three ETLs when incorporated into BaHfSe$_3$-based solar cells. AZnO-based devices reach a top PCE of 31.05% when configured with a 1.8 μm absorber and a 30 nm ETL, showcasing a favorable trade-off between efficiency and material economy. Notably, AZnO maintains good efficiency at reduced absorber thicknesses, making it a low-cost and easy-to-fabricate alternative. However, the devices with TiO$_2$ exhibit competitive performance, achieving a slightly higher maximum PCE of 31.08% with a thicker absorber layer of 2.1 μm. Its reliance on increased thickness implies a greater dependence on photon absorption to compensate for its reduced electron mobility. Conversely, WS$_2$ shows a lower overall efficiency, with a maximum PCE of 26.67% occurring at WS$_2$ thicknesses less than 0.15 μm combined with absorber thicknesses ranging from 1.8 to 2.1 μm.

There are several reasons for the noticeable differences in V_{OC}, J_{SC}, FF, and PCE across perovskite with various ETL. The absorption coefficient is a crucial component that greatly impacts photovoltaic metrics, including V_{OC}, J_{SC}, FF, and PCE. This parameter affects the coupling efficiency of light photons with the underlying CaHfSe$_3$ absorber layer and is directly correlated with the ETL's bandgap. The overall efficiency of the solar cell is significantly affected by the CBO, arising from the disparity in electron affinity and Fermi level positions between the absorber and the ETL.
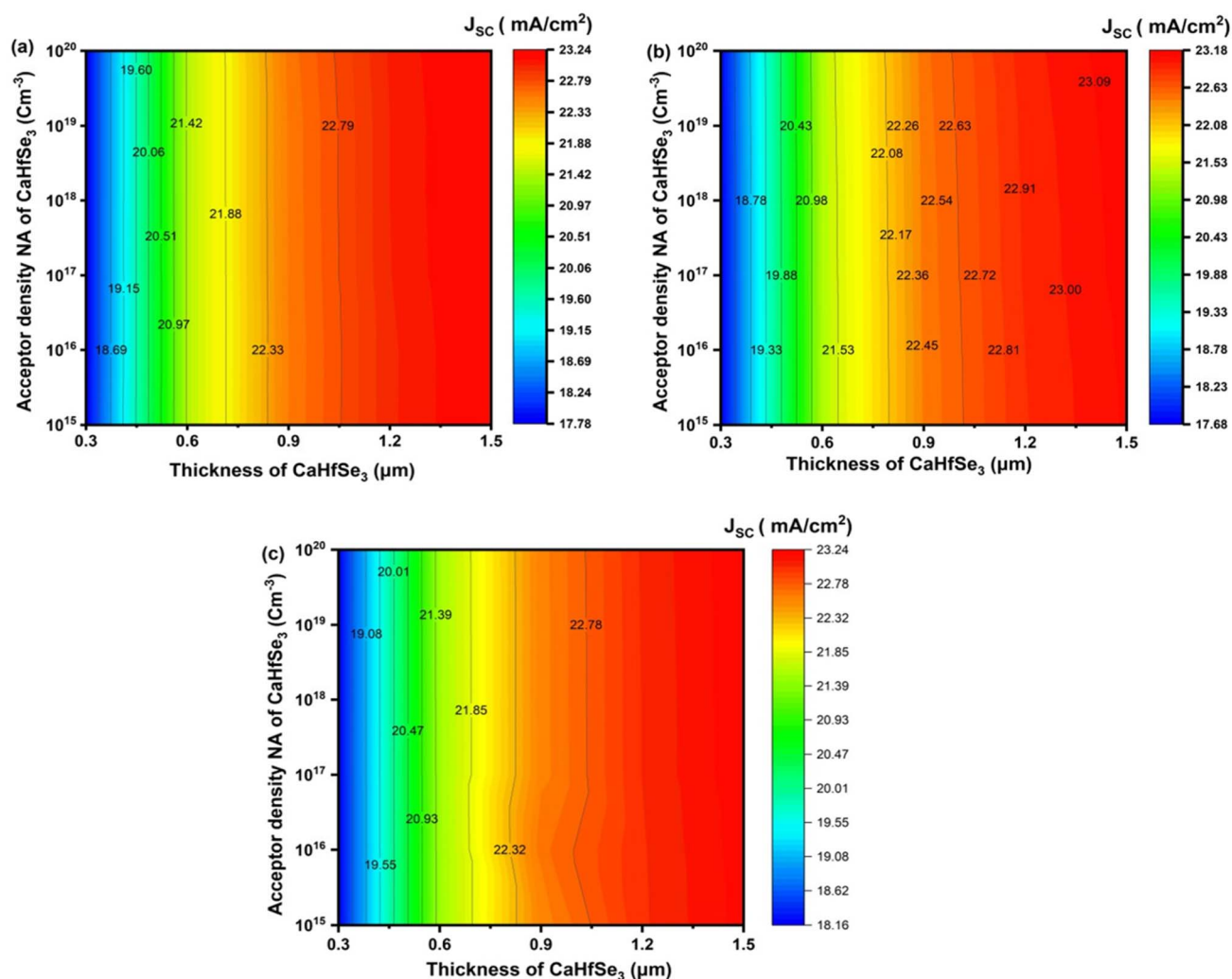

Fig. 9 Contour plots illustrate the influence of absorber doping concentration and thickness on J_{SC} for ETL types (a) AZnO, (b) TiO$_2$, and (c) WS$_2$.

3.4. Effect of absorber acceptor concentration and layer thickness on photovoltaic performance

Optimizing both the absorber thickness and N_A within the absorber is essential for achieving improved efficiency. To examine the impact of these factors, we conducted simulations by adjusting the acceptor doping density (N_A) from 1×10^{15} to 1×10^{20} cm^{-3} and absorber thickness from 0.3 to 1.5 μm across seven distinct PSC configurations. Fig. 8 shows how variations in absorber thickness and N_A influence the (V_{OC}) in the validated PSC configurations.

According to Fig. 8, under conditions where the absorber was less than 0.9 μm thick and the acceptor doping concentration (N_A) was fixed at 10^{20} cm^{-3}, AZnO and TiO$_2$ achieved their maximum V_{OC} values of 1.5 V. Notably, increasing the absorber thickness beyond this threshold resulted in a gradual decline in V_{OC} for all ETLs under the same doping conditions. The data's shape makes it evident that while V_{OC} tends to drop with increasing absorber thickness, it increases with increased

acceptor concentration (N_A). This behavior is explained by the stronger electric field and greater built-in potential at higher doping levels, which makes it easier to separate and remove photogenerated carriers and increase V_{OC}. Nevertheless, the series resistance rises, and the greater sheet resistance at thicker absorber layers constrains the hole mobility towards the HTL. This leads to a decrease in carrier collection and, thus, a lower V_{OC}.[25]

Fig. 9(a)–(c) show that the short-circuit current density J_{SC} for devices using ZnO, TiO$_2$, and WS$_2$ as ETL shows a significant increase with absorber thickness and a modest increase with increasing acceptor density (N_A). The maximum J_{SC} values of 23.239 mA cm^{-2}, 23.169 mA cm^{-2} and 23.232 mA cm^{-2} for ZnO, TiO$_2$, and WS$_2$, respectively, were observed at an absorber thickness of 1.5 μm with $N_A = 10^{20}$ cm^{-3}. The increased light absorption in the thicker CaHfSe$_3$ absorber layer, which permits a bigger production of photogenerated carriers, is primarily responsible for the progressive increase in J_{SC} seen for all ETLs from 0.3 μm to 1.5 μm. Furthermore, for a constant thickness,

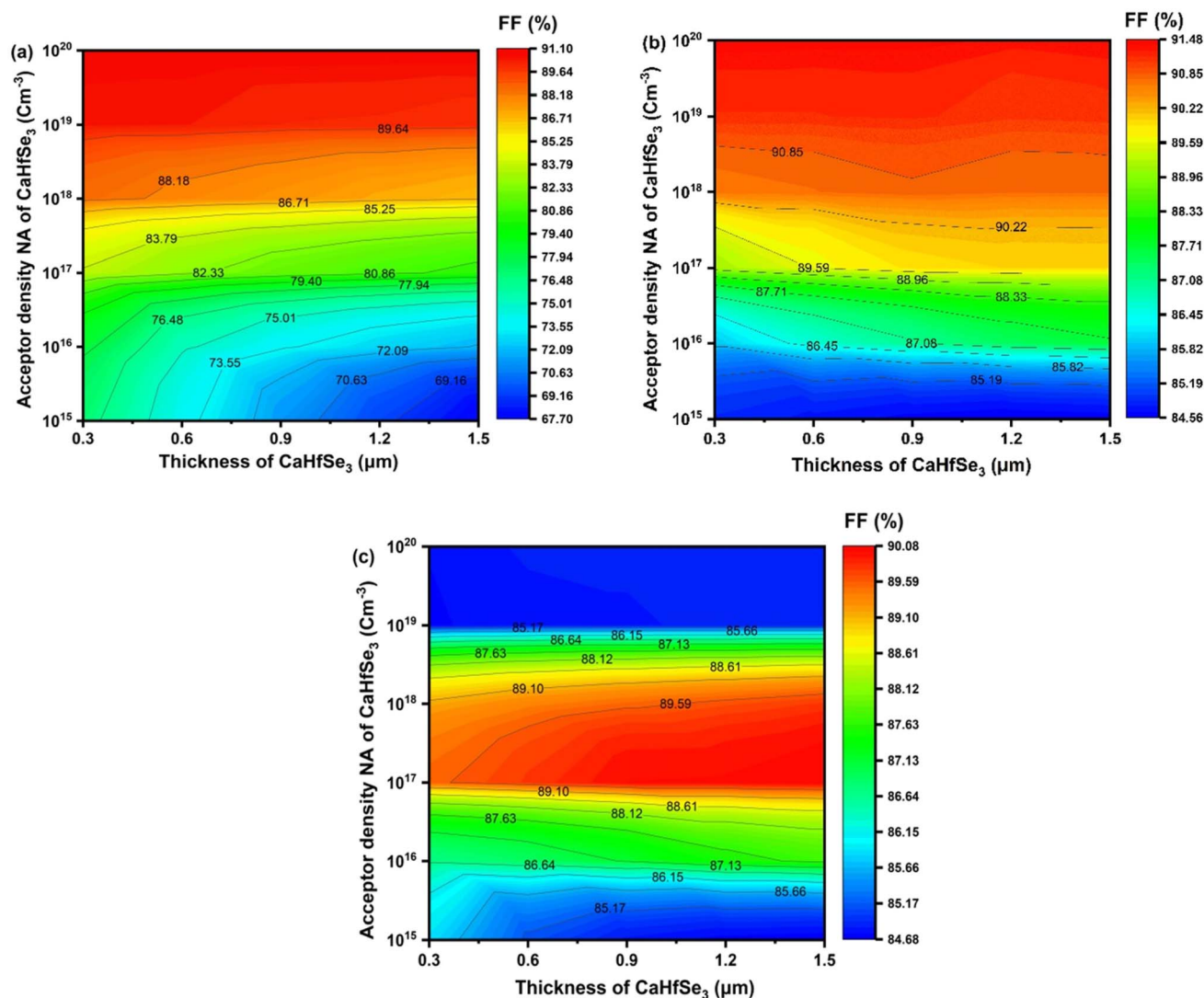**Fig. 10** Impact of (a) AZnO, (b) TiO$_2$, and (c) WS$_2$ ETLs on FF (%) contour plots in CaHfSe$_3$ perovskite solar cells.

the J_{SC} values are rather stable over N_A values and improve slightly with increasing N_A. This is explained by the improved separation of photogenerated carriers in highly doped materials, leading to more effective electric field generation and less recombination. Fig. 10(a)–(c) illustrate that, for all three ETLs, the fill factor (FF) typically increases with the rising acceptor density (N_A) throughout all examined thicknesses.

This enhancement results from minimized carrier recombination and enhanced charge transport as a result of increased doping levels. TiO$_2$ often demonstrates the highest fill factor values, achieving 91.48% at a minimal thickness of 0.3 μm and elevated doping levels ($N_A > 10^{19}$ cm^{-3}). This exceptional performance is attributed to its effective surface passivation characteristics and favorable band alignment with CaHfSe$_3$, which reduces non-radiative recombination. At low acceptor densities, AZnO exhibits lower FF values than TiO$_2$, but, when N_A rises, it shows notable improvement, reaching up to 91.03–91.06% for $N_A = 10^{20}$ cm^{-3}. However, we observe that the WS$_2$-based solar cell structure exhibits a maximum FF value,

reaching nearly 90% when the thickness of absorber exceeds 0.8 μm, and N_A ranges from 10^{17} to 10^{18} cm^{-3}.

Fig. 11(a) and (b) highlight the combined effect of absorber thickness and N_A on the performance of CaHfSe$_3$-based solar cells. The simulations show that the PCE reaches its peak at absorber thicknesses of 1.2 μm and 1.5 μm, achieving 32.30% for AZnO and 32.40% for TiO$_2$ when N_A exceeds 10^{19} cm^{-3}. A reduction in absorber thickness leads to a noticeable drop in PCE, since thinner layers allow a considerable fraction of incident photons to pass through unabsorbed, thereby limiting electron–hole pair generation. Conversely, thicker absorbers enhance light absorption, increase carrier generation, and result in higher efficiencies. In addition, the PCE improves with increasing N_A, as higher acceptor doping concentrations strengthen the built-in electric field, which facilitates the separation and transport of photogenerated carriers, reduces recombination losses, and ultimately enhances device performance.[26] Fig. 11(c) shows that using WS$_2$ as the ETL results in a PCE of 29.12% when the absorber thickness exceeds 1.2 μm

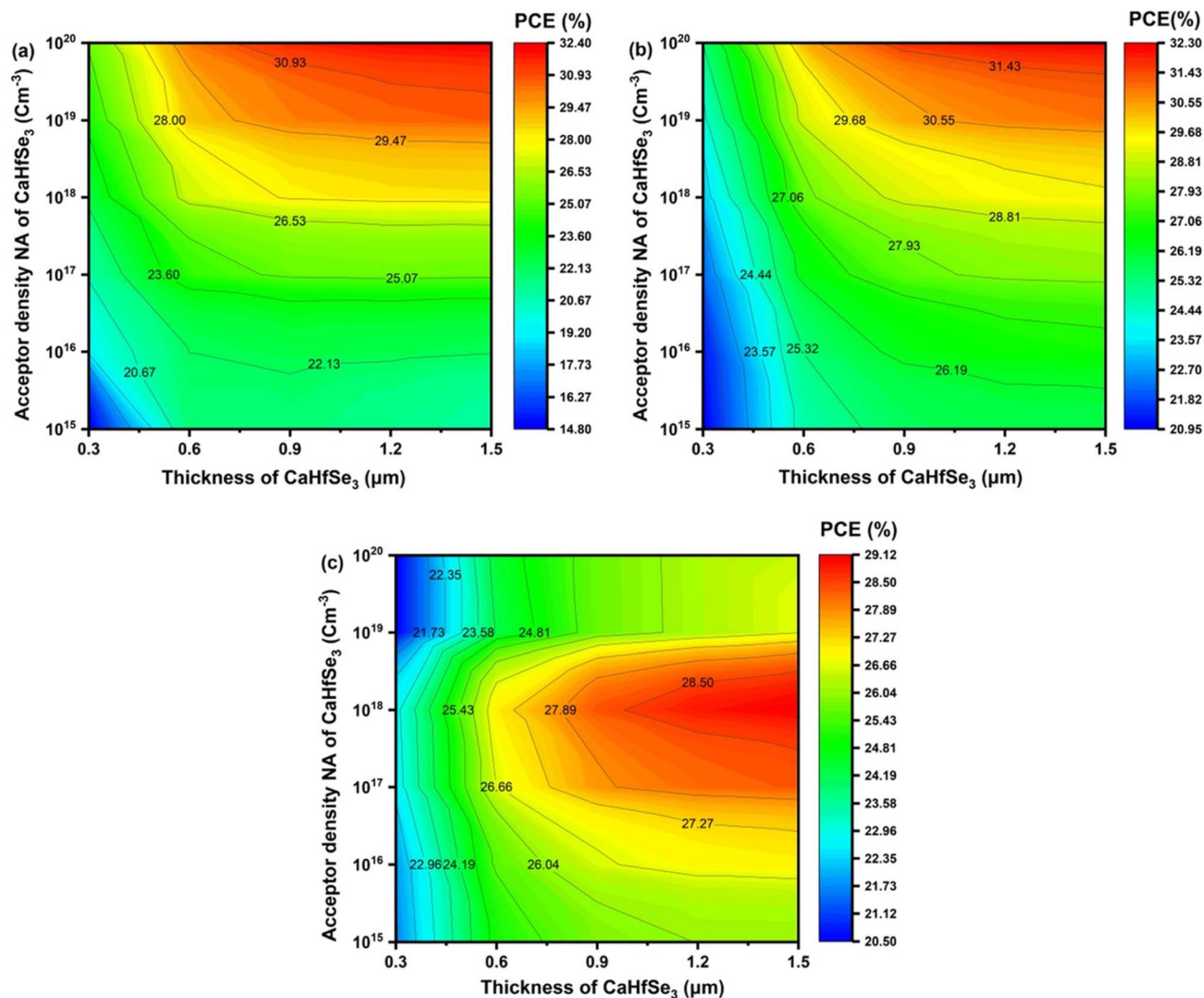Fig. 11 PCE (%) contour plots with ETL as (a)AZnO, (b) TiO$_2$, and (c) WS$_2$.

and the N_A is approximately 10^{18} cm^{-3}. This phenomenon occurs because a high acceptor density increases the recombination rate, restricting carrier mobility and subsequently reducing the PCE.

3.5. Influence of defect density and CaHfSe₃ layer thickness on photovoltaic performance

Defect density is a crucial factor that significantly impacts perovskite solar cells (PSCs). Absorber layer defects, acting as recombination sites, reduce carrier lifetimes and decrease device efficiency. Consequently, achieving excellent performance necessitates reducing the absorber layer's defect density. Numerous studies have focused on the interplay between defect density and absorber thickness in CaHfSe₃-based PSCs and their effect on device efficiency and the results demonstrate a significant relationship between the two factors. Optimizing both simultaneously can result in the most efficient device possible.

Hence, the thickness of the CaHfSe₃ absorber ranged from 300 nm to 1500 nm, alongside N_t values adjusted from 10^{13} to 10^{15} cm^{-3}. The simulation outcomes indicate that both the absorber thickness and N_t substantially affect the V_{OC} of

CaHfSe₃-based solar cells, as shown in Fig. 12. For all evaluated ETLs (AZnO, TiO₂, and WS₂), In configurations (a) and (b), V_{OC} exhibits a strong dependence on both thickness and defect density. When N_t is maintained below 10^{14} cm^{-3}, V_{OC} reaches values as high as 1.448 V, indicating minimal nonradiative recombination and efficient carrier extraction. The voltage increases with thickness up to approximately 0.9 μm, beyond which the gain plateaus, suggesting that additional thickness does not significantly enhance photogeneration or reduce recombination. This behavior reflects a balance between optical absorption and carrier diffusion length, where excessive thickness may introduce resistive losses or trap-limited transport without further improving voltage. As N_t increases beyond 10^{16} cm^{-3}, a pronounced decline in V_{OC} is observed, regardless of thickness. This trend highlights the detrimental impact of bulk and interfacial defects, which act as recombination centers and suppress quasi-Fermi level splitting. The steep voltage gradient across the defect density axis underscores the necessity of defect passivation strategies, such as surface treatments or compositional tuning, to preserve high V_{OC} values. In contrast, configuration (c) yields significantly lower V_{OC} values, ranging from 1.128 V to 1.148 V. The voltage remains relatively insensitive to
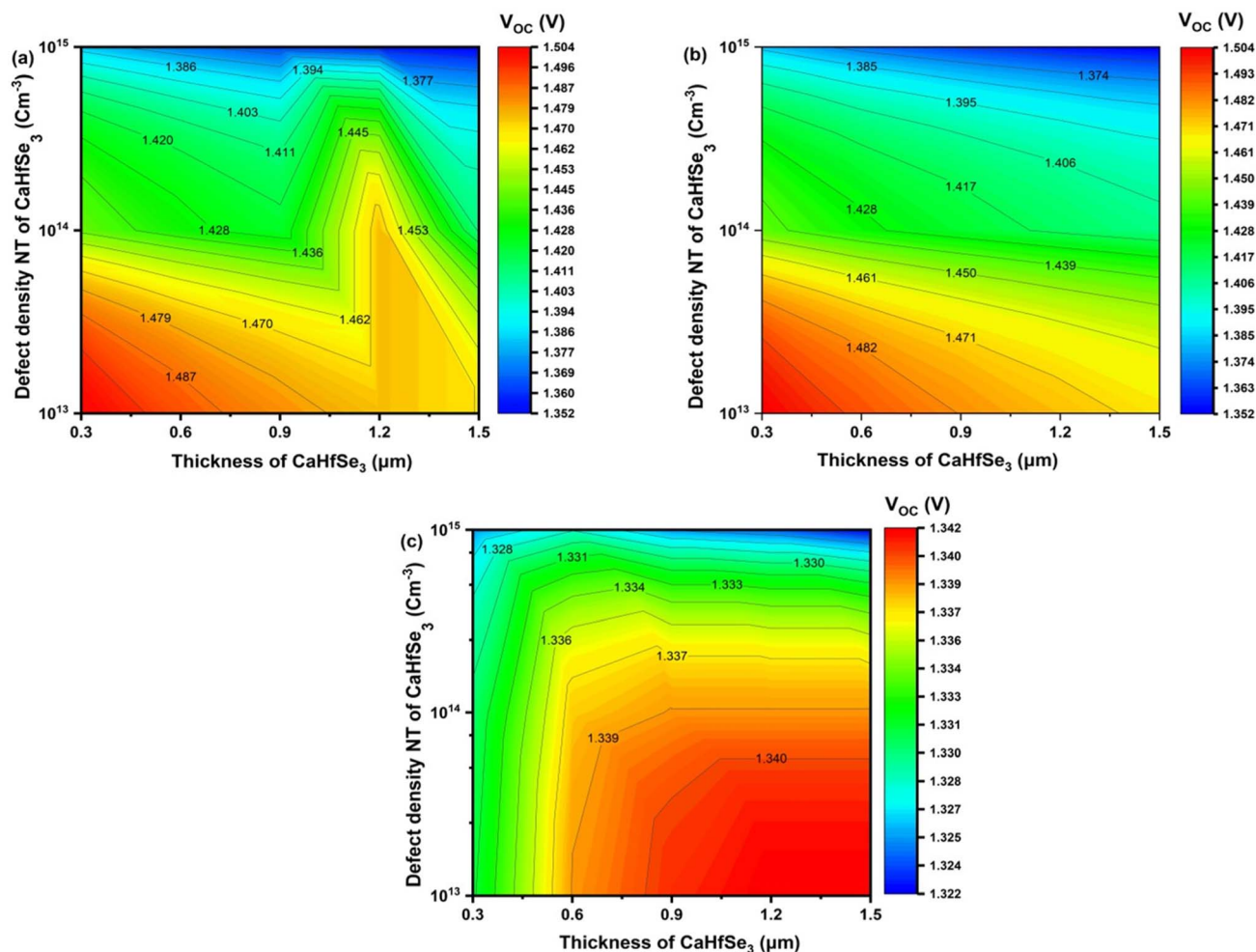

Fig. 12 Contour graphs of V_{OC} dependence on CaHfSe₃ absorber thickness and defect density with ETLs as (a) AZnO, (b) TiO₂, and (c) WS₂.

thickness variations, and even at low N_t, the performance is markedly inferior to that of configurations (a) and (b). This suggests a fundamentally different device architecture or material interface, potentially characterized by poor band alignment, high interface recombination velocity, or inadequate carrier selectivity. The suppressed V_{OC} may also reflect unfavorable energetics at the contact layers or the presence of deep-level traps within the CaHfS$_3$ matrix. Particularly at low defect concentrations ($N_t = 10^{13}$ cm^{-3}), since the longer carrier transport pathways raise the possibility of recombination. Furthermore, the greatest V_{OC} values reported are 1.504 V for both AZnO and TiO$_2$ at 0.3 μm thickness and $N_t = 10^{13}$ cm^{-3}, and 1.342 V for WS$_2$ at 1.2–1.5 μm thickness with the same low defect density.

Fig. 13 shows that the J_{SC} of CaHfSe$_3$-based solar cells is significantly influenced by both the absorber thickness and N_t. Because larger layers generate more carriers and absorb more photons, J_{SC} grows continuously with absorber thickness. Beyond 1.2 μm, this gain tends to saturate, suggesting an ideal thickness range for balancing recombination and absorption losses. On the other hand, J_{SC} slightly decreases when the defect

density is increased from 10^{13} to 10^{15} cm^{-3} at a given thickness. This is because greater trap-assisted recombination lowers the carrier collection efficiency. The maximum J_{SC} values recorded are 23.24, 23.02, and 23.24 mA cm^{-2} for AZnO, TiO$_2$, and WS$_2$, respectively. These values all correspond to a low defect density $<10^{14}$ cm^{-3} and an absorber thickness greater than 1.2 μm. These results validate that adequate absorber thickness and defect passivation are both necessary to maximize photogenerated current.

For the device utilizing AZnO as the electron transport layer, Fig. 14(a), the fill factor exhibited considerable stability across varying absorber thicknesses and defect concentrations. In particular, FF values were higher than 90.50% for thicknesses <900 nm and $N_t < 10^{15}$ cm^{-3}. The highest FF of 90.78% was observed at $N_t = 10^{13}$ cm^{-3} and thickness ~0.6 μm. At 1.2 μm thickness, FF decreased from 90.78% to 89.76% as N_t grew from 10^{13} to 10^{15} cm^{-3}, indicating a modest drop with rising N_t. Due to accumulated recombination. Thus, low N_t and thickness allow for better fill factor, especially internal losses. Furthermore, the TiO$_2$-based ETL device exhibited steady performance over diverse absorber thickness and N_t conditions, as presented

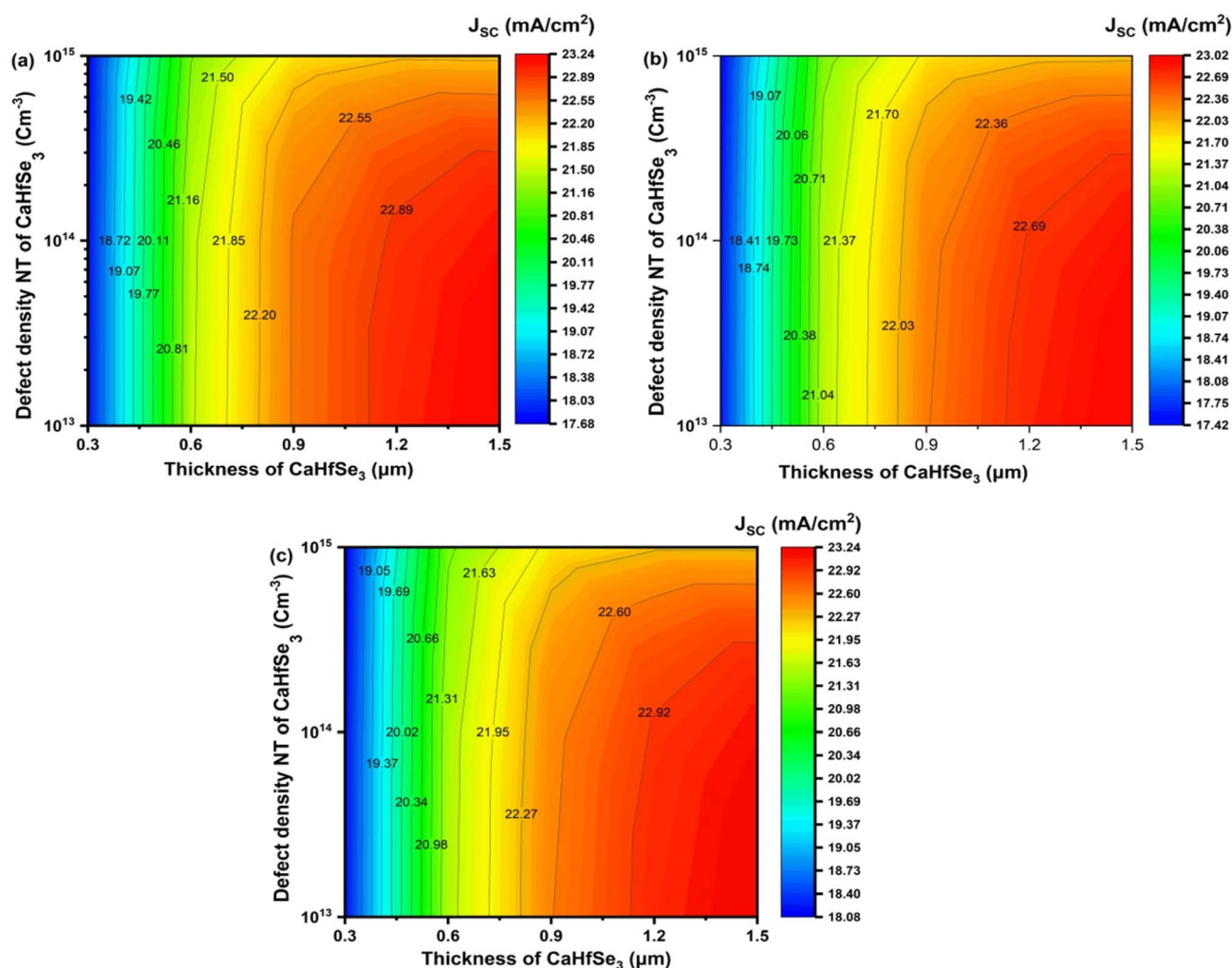**Fig. 13** Contour graphs of J_{SC} as a function of CaHfSe$_3$ absorber thickness and defect density with ETL as (a) AZnO, (b) TiO$_2$, and (c) WS$_2$.
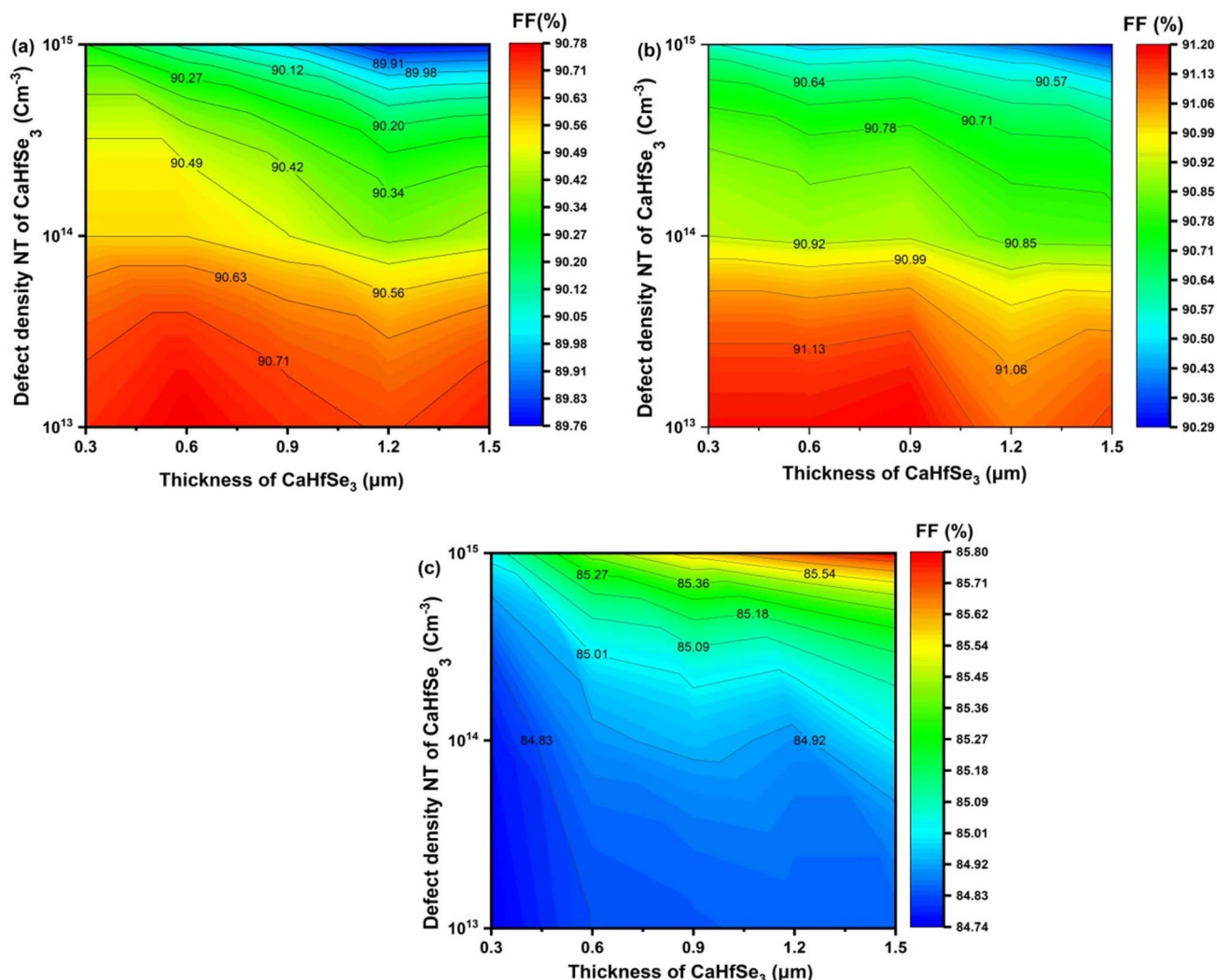
Fig. 14 Contour graphs of FF as a function of CaHfSe$_3$ absorber thickness and defect density with ETL as (a) AZnO, (b) TiO$_2$, and (c) WS$_2$.

in Fig. 14(b). A maximum fill factor (FF) of 91.20% was achieved at $N_t = 1.0 \times 10^{13}$ cm^{-3} and a thickness of 0.9 μm. As the defect density increased, the FF gradually declined; however, it remained above 90% under all tested conditions. This highlights the excellent compatibility of TiO$_2$ with the CaHfSe$_3$ absorber layer, as well as its effectiveness in minimizing series resistance and enabling efficient charge extraction.

In contrast, the device employing WS$_2$ as the ETL displayed a lower but increasing FF trend with absorber thickness. Fig. 14(c) indicates that FF rose from 85.04% to 85.80% as thickness increased from 0.3 μm to 1.5 μm at $N_t = 1.0 \times 10^{15}$ cm^{-3}, achieving a maximum FF of 85.80%. At low N_t values (<10^{14} cm^{-3}), FF stayed below 85.00%, suggesting that WS$_2$ is more suitable for thicker absorbers with higher defect tolerance. The lowest result, 84.74%, was recorded at 0.3 μm and $N_t = 1.0 \times 10^{13}$ cm^{-3}.

Fig. 15 shows the PCE of CaHfSe$_3$-based solar cells utilizing three different ETLs: AZnO, TiO$_2$, and WS$_2$, with various absorber thicknesses and defect densities. For all ETLs, the PCE increased with absorber thickness and dropped with increasing

defect density (N_t), which corresponded to improved light absorption and lower carrier recombination at low N_t. The device achieved a maximum PCE of 31.00% when AZnO served as the ETL, combined with a carrier concentration of 10^{13} cm^{-3} and an absorber thickness of 1.5 μm. Moreover, Fig. 15(b) shows that the device using TiO$_2$ as the ETL demonstrated high performance, achieving a maximum PCE of 30.81% under similar conditions. In contrast, Fig. 15(c) reveals that WS$_2$ exhibited a lower peak efficiency of 26.46% at N_t equals 1.0×10^{13} cm^{-3} and an absorber thickness of 1.5 μm. While both AZnO and TiO$_2$ showed high and comparable efficiencies across all examined conditions, WS$_2$ consistently delivered lower efficiencies, particularly at low thicknesses and high defect densities. This behavior may be attributed to increased interfacial recombination or higher series resistance. These findings underscore the excellent performance and compatibility of AZnO and TiO$_2$ as ETLs for CaHfSe$_3$-based devices, particularly when combined with low defect densities and optimized absorber thickness.
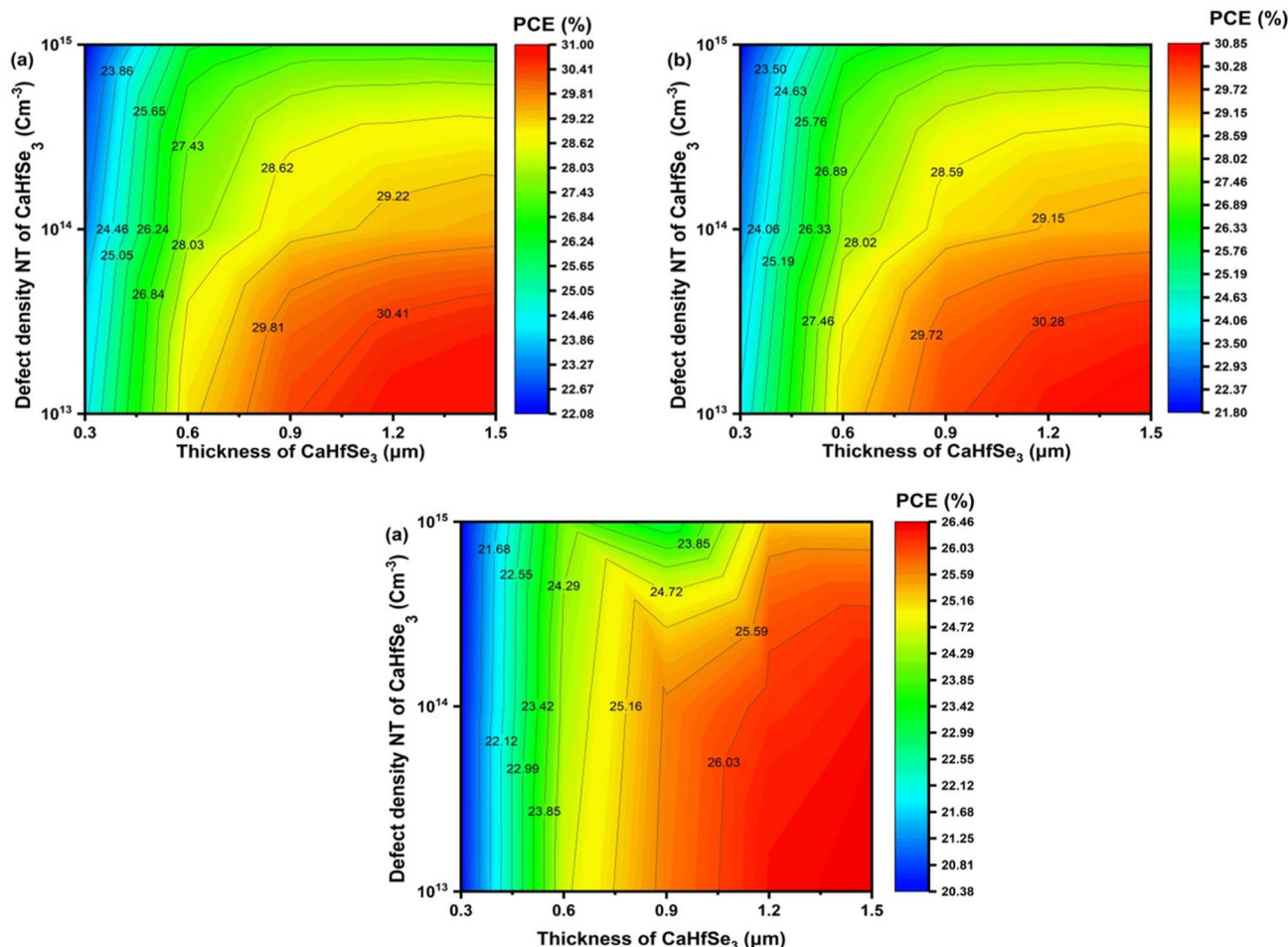
Fig. 15 PCE contour maps showing the influence of CaHfSe$_3$ absorber thickness and defect density for ETLs including (a) AZnO, (b) TiO$_2$, and (c) WS$_2$.

3.6. Effect of HTM and ETM thickness and carrier concentration on PV properties

3.6.1. Effect of HTM thickness. The HTL improves efficiency by collecting holes, restricting electron movement, and shielding the perovskite from environmental variables including moisture, heat, and oxygen.[27] This section uses AZnO as the ETM and MoO$_3$ as the HTM. HTL thickness was varied from 20–180 nm to evaluate how thickness influences the performance of a CaHfSe$_3$-based PSC. Fig. 16 shows that all the significant metrics for performance, namely V_{OC}, J_{SC}, FF and PCE, were not significantly affected over the range of thicknesses and showed only slight differences in overall performance. Specifically, V_{OC} = 1.482 V, J_{SC} = 22.575 mA cm^{-2}, FF = 90.73% and PCE = 30.37%. Overall, the MoO$_3$ layer provided a suitable energy level for hole transport and sufficient holes across the range of HTL thickness without adding series resistance, or introducing any optical losses. Even the lowest thickness was suitable in ensuring effective hole extraction and hole transport (30 nm), as evidenced from the data showing that the performance metrics were not generally influenced by HTL thickness. Therefore, reduced HTL thickness is a solution to cut

material usage or production cost while remaining similar in efficacy (Fig. 17).

3.6.2. Impact of the concentration of HTM carriers. The results indicate that V_{OC} (1.482 V) and J_{SC} (22.575 mA cm^{-2}) remain almost unchanged with increasing N_A. This stability arises because these parameters are primarily governed by the absorber's intrinsic optoelectronic properties, including bandgap, absorption coefficient, and carrier lifetime which are not significantly affected by moderate changes in the MoO$_3$ HTL doping level. Consequently, carrier generation, separation, and transport within the absorber remain stable, in agreement with previous simulation studies on the limited effect of HTL doping on V_{OC} and J_{SC}. However, the FF shows a slight improvement, rising from 90.39% to 90.73% as N_A increases. The improvement is probably caused by increased hole transport efficiency and reduced series resistance at the HTL, owing to higher doping levels, enabling better charge extraction. The PCE rises from 30.26% to 30.36%, plateauing above a doping concentration of 10^{15} cm^{-3}.

3.6.3. Impact of the concentration of ETM carriers. Fig. 18 illustrates the influence of the ETL donor doping density (N_D) on the photovoltaic performance of solar cells utilizing TiO$_2$,
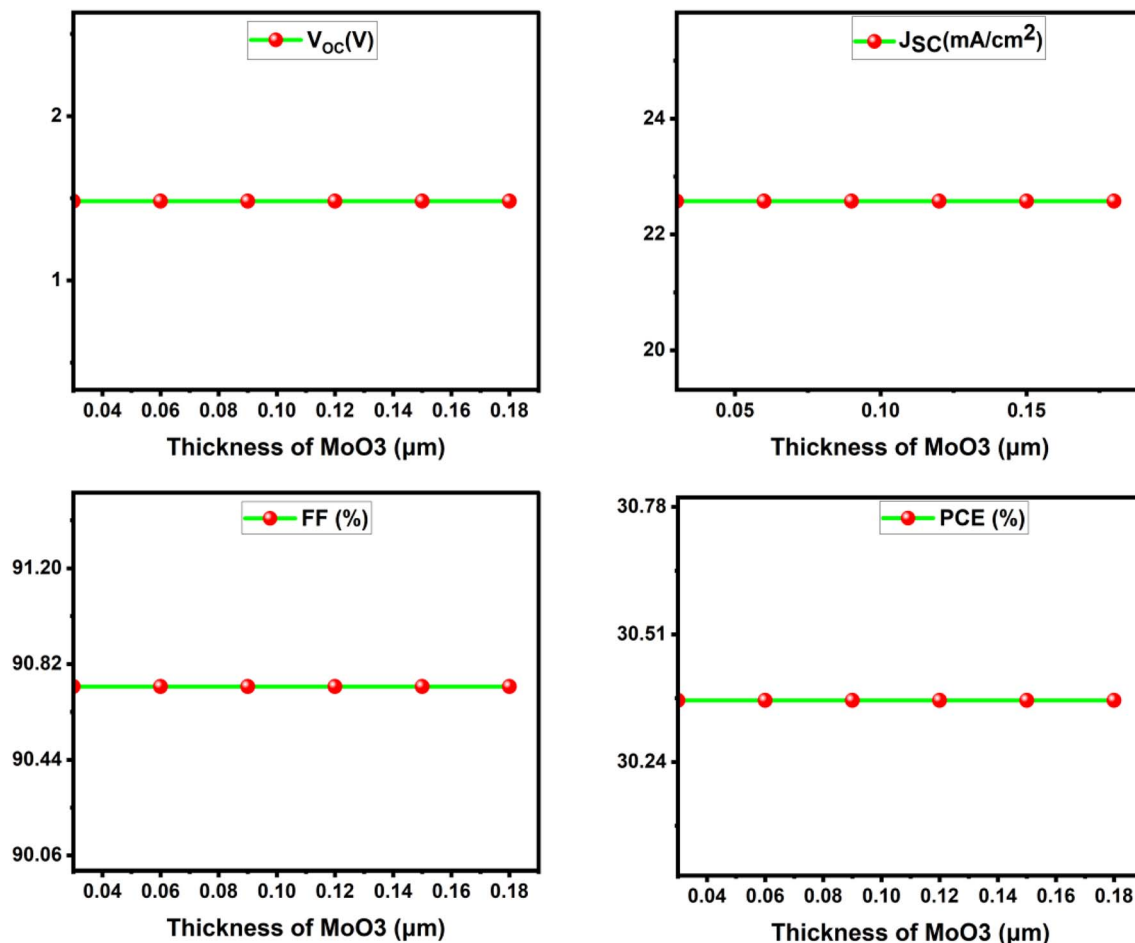
Fig. 16 Influence of MoO$_3$ layer thickness on the solar cell photovoltaic characteristics.

ZnO, and WS$_2$. TiO$_2$ demonstrates consistent characteristics at all doping levels, maintaining a steady PCE of 30.41%, thus affirming its durability. Furthermore, AZnO shows a slight improvement in fill factor and efficiency as N_D increases, achieving a maximum power conversion efficiency of 30.48%. However, WS$_2$, with a maximum efficiency of 25.71%, demonstrates poorer and more doping-sensitive performance. In contrast V_{OC} is mainly determined by the absorber bandgap and the splitting of the quasi-Fermi levels, which are controlled by carrier generation and recombination within the absorber. Since ETL doping does not directly affect these intrinsic mechanisms, V_{OC} remains unchanged. Similarly, J_{SC} is governed by photon absorption and the diffusion/collection of photogenerated carriers in the absorber. ETL doping does not alter the absorption spectrum or the intrinsic carrier generation, so J_{SC} also stays constant (Fig. 19).

3.7. Impact of series resistance on performance

The series resistance (R_S) in a solar cell generally arises from three sources: carrier transport within the emitter and base layers, contact resistance at the metal–semiconductor interfaces, and the resistance of the front and rear metallic contacts. Minimizing R_S is crucial, as high values cause internal voltage drops that reduce the fill factor (FF) and overall power conversion efficiency (PCE). Excessive resistive losses can significantly reduce the fill factor. In the current investigation, when R_S escalates from 0 to 6 Ω cm^2, V_{OC} and J_{SC} stay rather stable throughout all ETLs, however, the FF and PCE diminish gradually. TiO$_2$ and AZnO show excellent starting efficiencies of 30.93% and 30.80%, respectively, which decline to 27.83% and 27.72% at the maximum R_S. WS$_2$ starts at a lower PCE of 26.60%, dropping to 23.63%. This demonstrates that increasing series resistance affects device performance largely *via* lowering FF.

3.8. Impact of shunt resistance on performance

The shunt resistance (R_{SH}) corresponds to leakage pathways through defects, pinholes, or imperfect interfaces. A low R_{SH} leads to significant losses in open-circuit voltage (V_{OC}) and a decrease in FF, whereas a high R_{SH} ensures that the majority of photogenerated carriers contribute to power output. The influence of shunt resistance (R_{SH}) on the photovoltaic performance
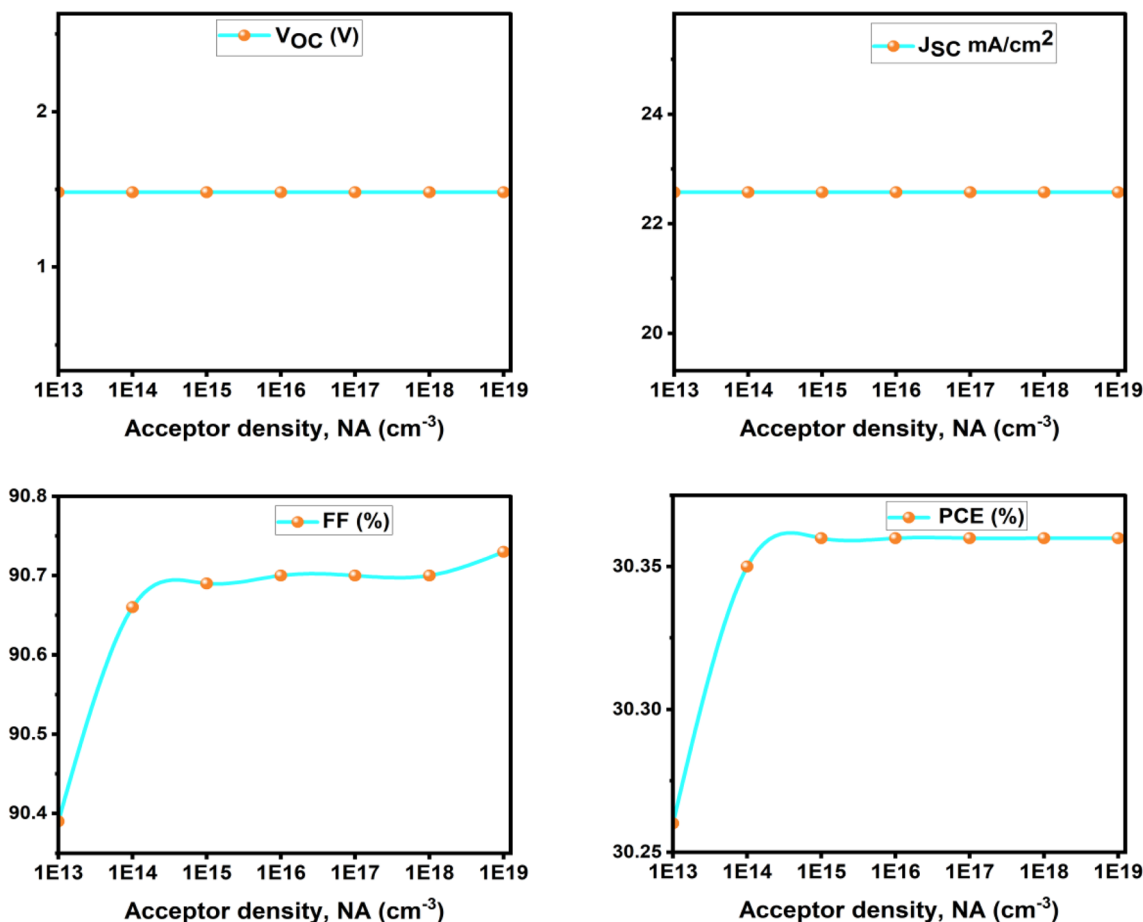
Fig. 17 Effect of MoO$_3$ acceptor doping concentration (N_A) on photovoltaic parameters.

of solar cells using AZnO, TiO$_2$, and WS$_2$ as electron transport layers (ETLs) was studied. Fig. 20 shows that raising R_{SH} from 100 to 900 Ω cm^2 significantly improved FF and PCE across all configurations. This behavior is explained by suppressing leakage currents, which are usually linked to manufacturing flaws, and avoiding the junction using low-resistance shunt routes. In particular, when R_{SH} rose, FF for the AZnO-based device improved from 40.59% to 84.71%, and PCE improved from 13.59% to 28.88%. At $R_{SH} = 900$ Ω cm^2, the TiO$_2$- and WS$_2$-based cells showed comparable improvements, with final PCE values of 28.74% and 25.05%, respectively. The fill factor is the metric most sensitive to changes in shunt resistance, as seen by the relatively consistent V_{OC} and J_{SC} over the R_{SH} range.

3.9. Effect of temperature

One of the most difficult issues with PSC is guaranteeing its long-term stability, particularly at high temperatures. High temperatures can induce chemical and structural changes in perovskite materials, leading to a significant reduction in device performance. Furthermore, thermal stress may damage the integrity of the interfaces between distinct layers, causing greater charge carrier recombination and impeding charge transfer.[28] To better understand the thermal response of PSC in actual working situations, a rigorous performance study was performed across a temperature range of 300 K to 400 K. Fig. 21. It has been demonstrated that increasing the temperature (from 300 to 400 K) reduces the V_{OC}, fill factor (FF), and PCE, while the J_{SC} remains essentially constant. This drop is mostly because of more recombination and energy loss at high temperatures, making removing charges and lowering the potential difference across the cell. TiO$_2$ and AZnO have similar performance, with V_{OC} values of 1.48 V, PCEs surpassing 30% at 300 K, and strong thermal stability. WS$_2$ had lower results (V_{OC} of 1.34 V, PCE ~25.7%) and more noticeable deterioration with temperature, indicating inefficient charge extraction and higher recombination. In contrast, the simulated J_{SC} remains nearly constant between 300 K and 400 K because photon absorption and carrier generation in the absorber are not significantly affected by temperature, while temperature mainly influences V_{OC} through the increase of the saturation current density.

3.10. Examination of the rates of recombination and generation

Elevating electrons from the B$_V$ to the B$_C$ causes holes to develop in the valence band, which in turn creates electron–hole pairs. This process is the essential mechanism for creating charge carriers in the substance. In SCAPS-1D, the generation rate $G(x)$ is determined by the input photon flux N_{phot} (λ,x),
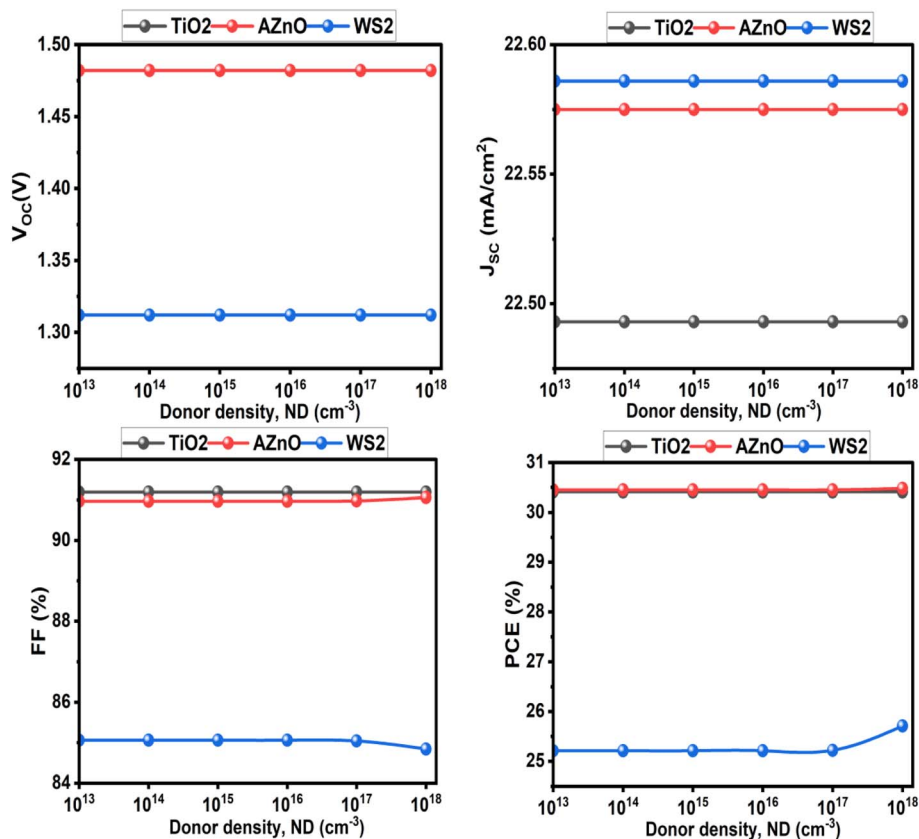
Fig. 18 Effect of ETM donor doping concentration (N_D) on photovoltaic parameters.

which indicates the quantity of photons accessible for absorption at each depth x and wavelength λ. This photon flux is utilized to estimate the spatial generation profile within the absorber layer according to eqn (7):

$$G(\lambda,x) = \alpha(\lambda, x) \cdot N_{phot}(\lambda, x) \qquad (7)$$

It is essential to integrate insights from carrier generation-recombination mechanisms and band structure studies to optimize absorber thickness, doping levels, and interface engineering, while selecting suitable ETLs and HTLs. This comprehensive knowledge enhances the efficiency, stability, and overall performance of CaHfSe$_3$-based solar cells. Fig. 22 illustrates carrier generation and recombination rates at various depths (0 to 1.1 μm) in three CaHfSe$_3$-based CP solar cells. Investigations indicate that generation rates for all devices peak between 0.15 and 0.3 μm. In contrast, the recombination rate acts as a limiting factor, neutralizing these electron–hole pairs and preventing them from increasing the photocurrent. Carrier density and lifespan are the primary factors influencing the recombination rate. Moreover, defects present within the absorber and at its interfaces considerably increase the rate of electron–hole recombination. These imperfections, often caused by impurities, structural faults, or grain boundaries, lead to a non-uniform distribution of the recombination rate across the material. The PSC with WS$_2$ and AZnO ETL had the

greatest recombination rates in the 1 to 1.1 μm range, where AZnO as the ETL exhibited the highest rate. This occurs when additional electrons in the B$_C$ bridge the E_g and join the B$_V$, becoming stable and taking the position of a hole.

3.11. Back contact effect on PV parameters

Eight distinct metals were used as rear electrodes (Table 3). In simulations for structure based on FTO/AZnO/CaHfSe$_3$/MoO$_3$, exhibiting work function values spanning from 4.65 to 5.70 eV, to assess the impact of the back contact Work function on device performance. The results are summarized in Fig. 23. It has been discovered that the PCE improves with an increasing work function, eventually reaching a saturation point of roughly 5.2 eV. At lower levels, the reduced PCE results from creating a Schottky barrier at the metal/absorber interface, which prevents effective hole extraction and promotes interfacial recombination. Furthermore, as the work function exceeds ~5.0 eV, the energy alignment at the back contact becomes more favorable for hole transport, lowering barrier height and improving carrier extraction. This leads to a fast rise in efficiency, reaching a maximum of around 30.37%. Beyond this level, the device's performance plateaus, indicating that the contact performs ohmically. Significantly, while gold ensures superior device performance, it accounts for around 20% of the overall production cost in perovskite solar cells. Electrodes
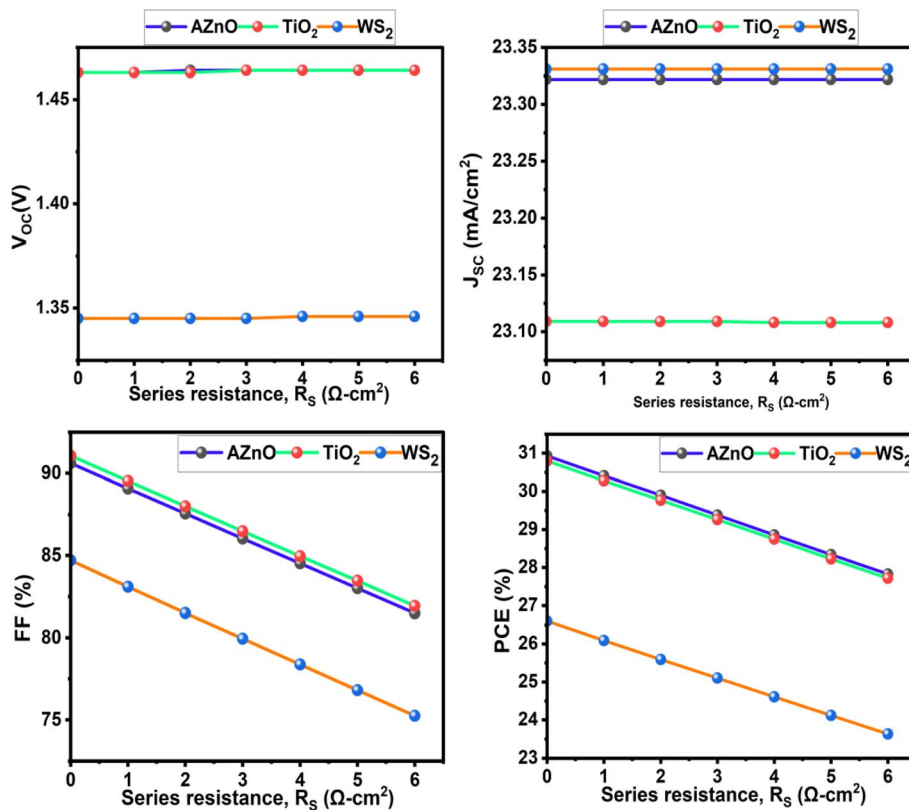
Fig. 19   The impact of series resistance on solar cell performance under varied ETLs.
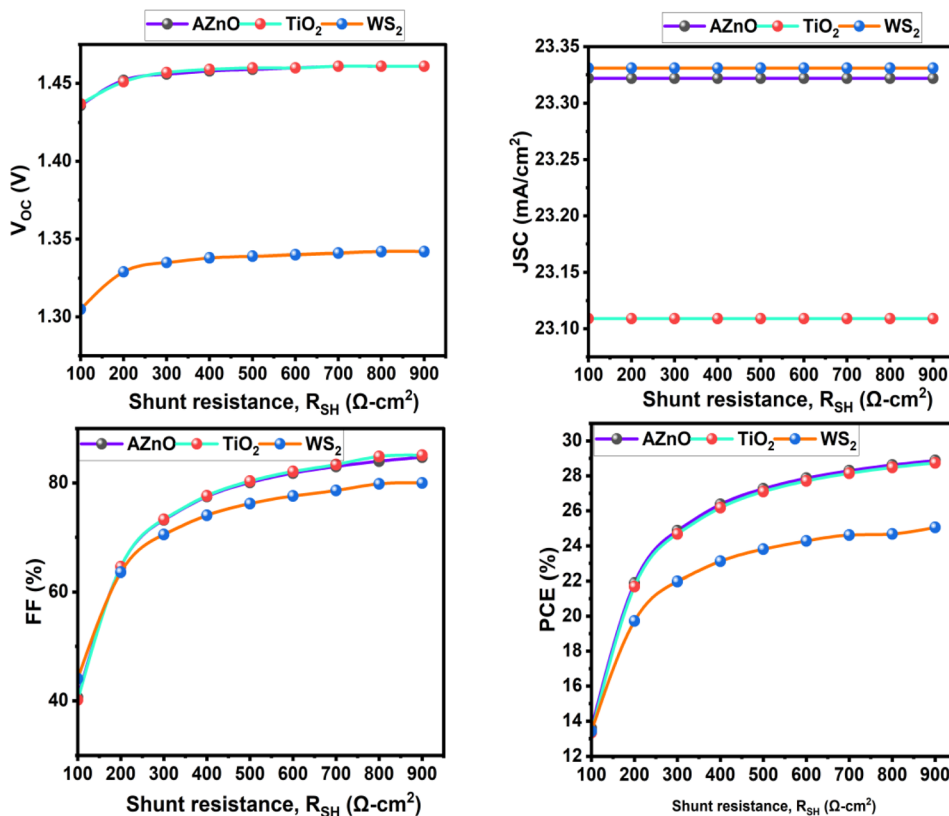

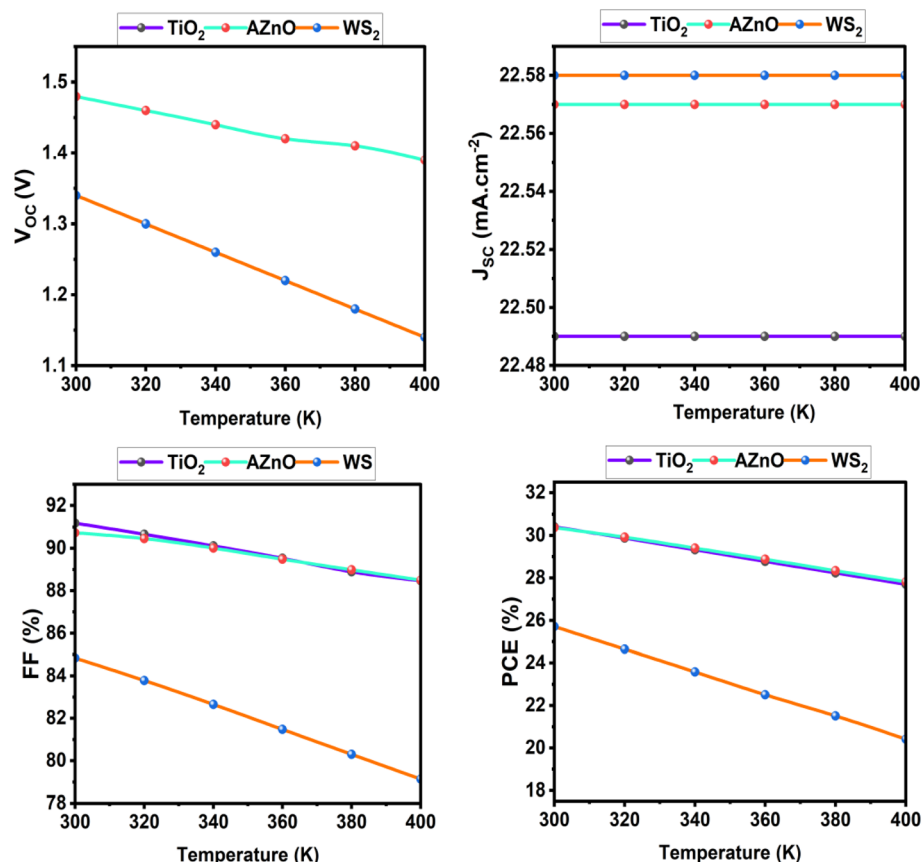Fig. 20   Effect of R_{SH} on the PSCs parameters.

Fig. 21 Impact of temperature on solar cell performance using TiO_2, AZnO, and WS_2 as ETLs.

composed of Ni, Pd, and Pt provide cost-effective alternatives, demonstrating promising efficiency levels that render them feasible substitutes for Au without significantly compromising device performance.

3.12. Quantum efficiency and *J–V* properties

The current–voltage characteristics of the simulated devices are illustrated in Fig. 24(a). All three devices exhibited relatively high short-circuit current densities ($J_{SC} \sim 22.49$–22.58 mA cm^{-2}), indicating that the $CaHfS_3$ absorber effectively captures light and generates carriers. However, there are significant differences in overall current stability and open-circuit voltage (V_{OC}). The cell utilizing AZnO as the ETL maintains a stable current plateau across a wide voltage range and achieves the highest V_{OC} (≈ 1.46 V). This suggests reduced interfacial recombination losses and excellent band alignment at the AZnO/$CaHfS_3$ interface, indicating that AZnO is the most effective ETL among those studied. Fig. 24(b) shows how wavelength affects quantum efficiency (QE) for our investigation's three most successful devices. According to the data, AZnO and WS_2 outperform TiO_2 in the UV (300–360 nm) region, with QE values exceeding 90% compared to TiO_2,

approximately 60%. This improvement may be attributed to the superior electrical and optical characteristics of AZnO and WS_2, such as their broad band alignment compatibility with $CaHfS_3$ and high optical transparency in the ultraviolet region, resulting in more effective charge carrier extraction in the high-energy area. Within the visible spectrum (360–700 nm), all three ETL designs demonstrate virtually optimal quantum efficiency, with values around 100%. This suggests that the $CaHfS_3$ absorber efficiently transforms visible light photons into charge carriers and that the ETLs retain good charge transport with negligible recombination losses throughout this range. However, after 700 nm, the QE starts to drop dramatically for all setups. $CaHfS_3$'s bandgap limits its ability to absorb low-energy photons in the near-infrared range, causing a noticeable drop at 770–800 nm.

3.13. Comparing SCAPS-1D results with earlier research

A comparison with previously reported perovskite-based devices is summarized in Table 4. The FTO/TiO_2/$CaHfSe_3$/MoO_3/Au and FTO/AZnO/$CaHfSe_3$/MoO_3/Au devices developed in this study exhibit outstanding photovoltaic performance, with $V_{OC} \approx$ 1.52 V, $J_{SC} \approx$ 23.17–23.23 mA cm^{-2}, and PCE values exceeding
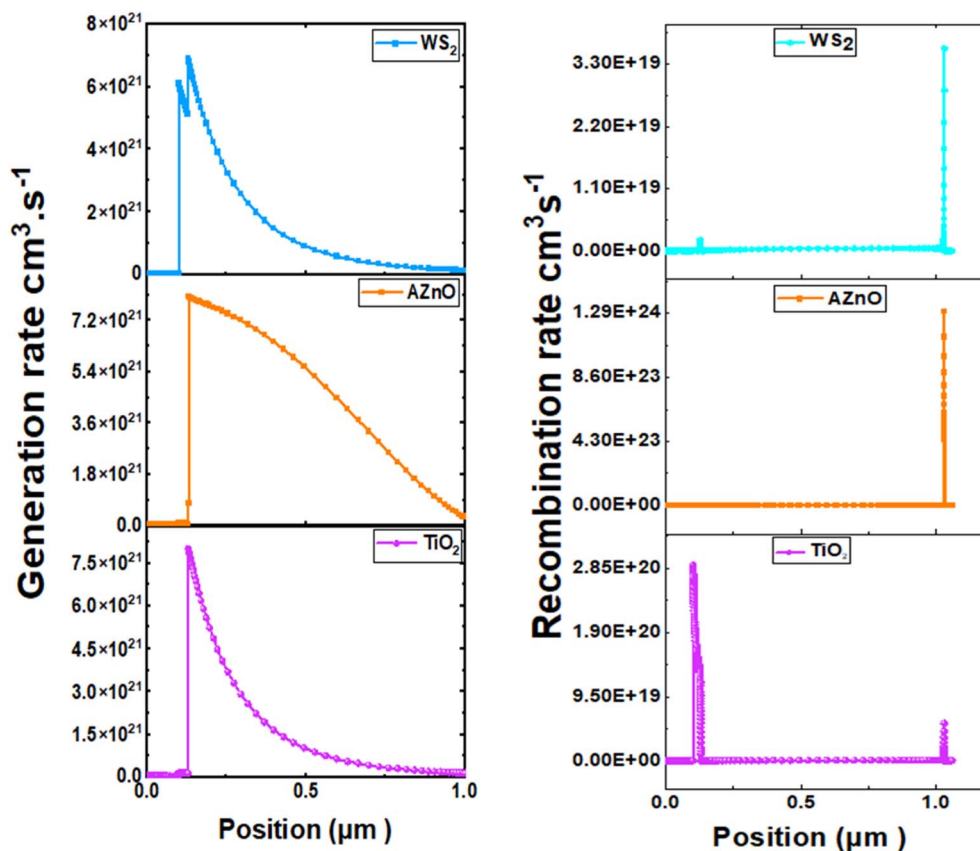
Fig. 22 Generation and recombination profiles in CaHfSe$_3$ absorber using TiO$_2$, AZnO, and WS$_2$ as ETLs.

Table 3 The contacts used in the setups and their work function

Back electrode	Cu	Fe	C	Au	W	Ni	Pd	Pt
Work function (eV) (ref. 29)	4.65	4.82	5.00	5.30	5.22	5.50	5.60	5.70

32%. The TiO$_2$-based structure achieves a slightly higher fill factor (91.41% *vs.* 91.02%) and overall efficiency (32.39% *vs.* 32.20%) compared to the AZnO-based device, reflecting lower resistive losses and more efficient charge extraction. These PCEs are significantly higher than those reported in previous studies, particularly for systems using CaHfSe$_3$ as the absorber layer. The top-performing FTO/TiO$_2$/CaHfSe$_3$/MoO$_3$/Au device, achieving 32.39% efficiency, highlights the superior optoelectronic properties of CaHfSe$_3$ and its favorable energy alignment with MoO$_3$. These results confirm the strong potential of the proposed materials and device architecture for high-performance, lead-free thin-film solar cells.

3.14. Validation against the ideal cell model

A comparison was made between the simulated photovoltaic properties of CaHfSe$_3$-based solar cells and those of an ideal single-junction solar cell. The optimized combination, FTO/TiO$_2$/CaHfSe$_3$/MoO$_3$/Au, attained a remarkable PCE of 32.39%, with a V_{OC} of 1.52 V, a J_{SC} of 23.17 mA cm^{-2}, and an FF of 91.41%. This indicates that the results conform to the
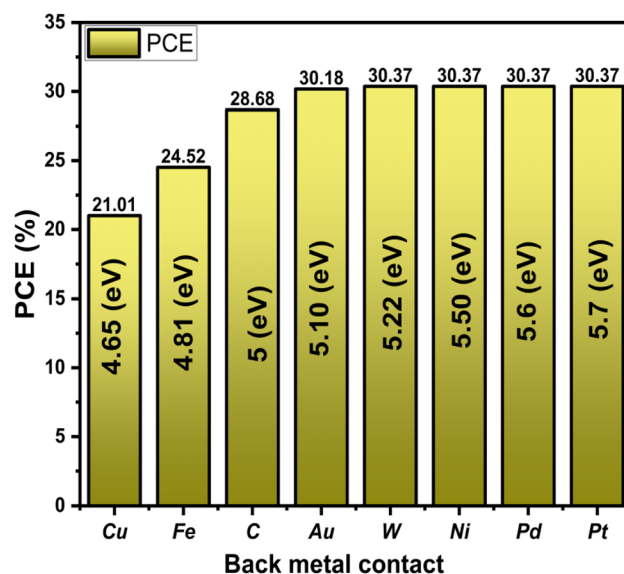

Fig. 23 Influence of the back electrode work function on solar cell PCE.
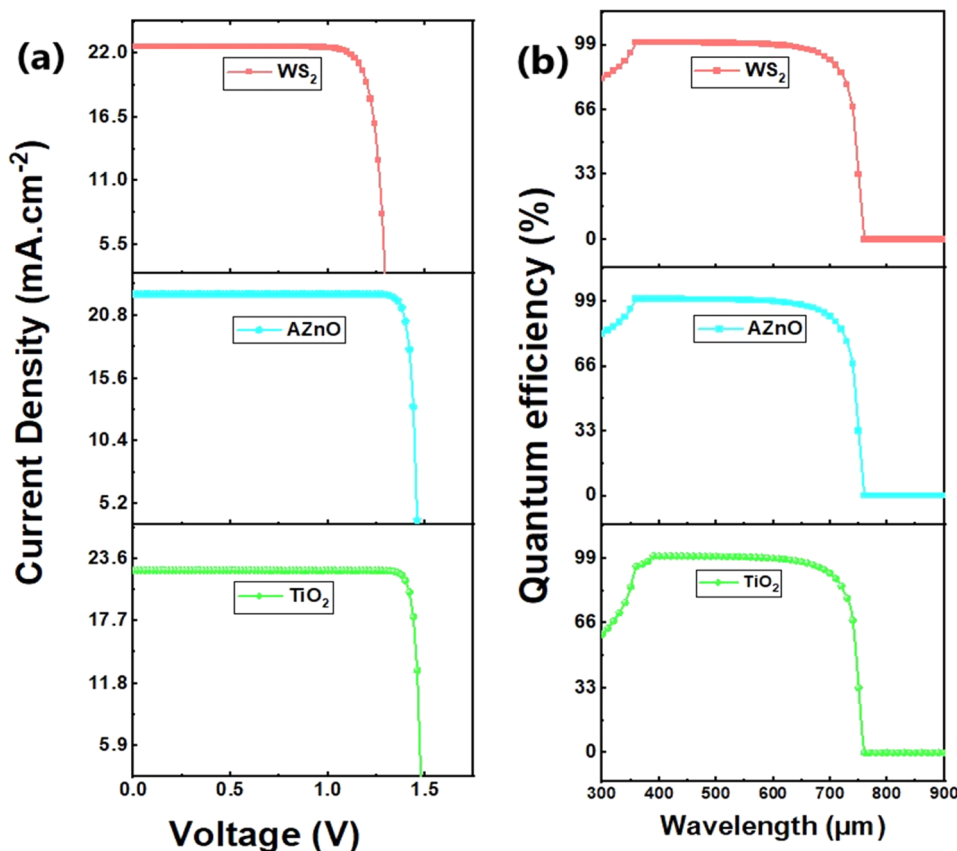
Fig. 24 (a) J–V characteristics and (b) quantum efficiency for every device under study.

Table 4 Device comparison: V_{OC}, J_{SC}, FF, and PCE

Structure	V_{OC} (V)	J_{SC} (mA cm^{-2})	FF (%)	PCE (%)	Year	Ref.
FTO/TiO$_2$/CaHfSe$_3$/MoO$_3$/Au	1.52	23.169	91.41	32.39	—	—
FTO/AZnO/BaHfSe$_3$/MoO$_3$/Au	1.52	23.23	91.02	32.20	—	—
FTO/WS$_2$/BaHfSe$_3$/MoO$_3$/Au	1.34	23.22	84.85	29.12	—	—
FTO/TiO$_2$/CaHfSe$_3$/NiO$_2$/Au	1.30	20.62	83.78	22.58	2025	19
FTO/TiO$_2$/BaZrS$_3$/SpiroOMeTAD/Au	0.70	22.00	79.40	12.42	2023	30
FTO/TiO$_2$/CaZrS$_3$/CuO	0.60	35.73	80.88	17.53	2024	18

theoretical boundaries of an ideal single-junction solar cell.[31] These results demonstrate the great promise of CaHfSe$_3$ as an absorber material for lead-free perovskite solar cells, since they approach the theoretical Shockley Queisser limit.

4. Conclusion

This makes our study unique as it intends to examine the photovoltaic characteristics of CaHfSe$_3$ absorber material in state-of-the-art solar cells. We explored the potential of devices constructed FTO/TiO$_2$, AZnO and WS$_2$ layers with CaHfSe$_3$/MoO$_3$/Au using SCAPS-1D simulations. We then analysed the effects of the absorber thickness, the density of defects in the absorber, carrier concentration in electron & hole transport layers, levels of acceptor doping, *etc.*, and how these factors impact the efficiency of the devices. The effects of R_S and R_{SH},

and temperature of operation in addition to other variables explored, were also examined in relation to overall photovoltaic performance. A detailed study of the band structure, carrier generation and recombination rates, J–V characteristics, and quantum efficiency (QE) was presented herein. The optimized device structure FTO/TiO$_2$/CaHfSe$_3$/MoO$_3$/Au yielded a power conversion efficiency (PCE) of 32.39%, with a V_{OC} of 1.52 V, J_{SC} of 23.17 mA cm^{-2}, and fill factor (FF) of 91.41%. In contrast, the FTO/AZnO/CaHfSe$_3$/MoO$_3$/Au structure had a PCE of 32.20% with near identical electrical properties. Overall, the results suggest the high optoelectronic quality of CaHfSe$_3$, and its compatibility with multiple ETLs. Additionally, cheap substitutes for gold in the back contact were examined, including carbon, with only modest losses in efficiency. Overall, this detailed and systematic work contributes to the understanding

of CaHfSe₃-based perovskite solar cells. It represents a potential pathway towards a lead-free, efficient, low-cost, and sustainable photovoltaic technology, and will support clean energy targets of the future.

Conflicts of interest

The authors declare no conflict of interest.

Data availability

The data will be available from the corresponding author on reasonable request. SCAPS-1D is available from https://scaps.elis.ugent.be/.

References

1 A. Basem, S. Opakhai, Z. M. S. Elbarbary, F. Atamurotov and N. E. Benti, A comprehensive analysis of advanced solar panel productivity and efficiency through numerical models and emotional neural networks, *Sci. Rep.*, 2025, **15**(1), 259.

2 H. Togun, A. Basem, M. J. Jweeg, N. Biswas, A. M. Abed, D. Paul, H. I. Mohammed, A. Chattopadhyay, B. K. Sharma and T. Abdulrazzaq, Advancing organic photovoltaic cells for a sustainable future: The role of artificial intelligence (AI) and deep learning (DL) in enhancing performance and innovation, *Sol. Energy*, 2025, **291**, 113378.

3 W. Li, Z. Xu, Y. Yan, J. Zhou, Q. Huang, S. Xu, X. Zhang, Y. Zhao and G. Hou, Passivating contacts for crystalline silicon solar cells: an overview of the current advances and future perspectives, *Adv. Energy Mater.*, 2024, **14**(18), 2304338.

4 F. A. Nelson, A. Basem, D. J. Jasim, T. E. Gber, M. T. Odey, A. F. Al Asmari and S. Islam, Chemical effect of alkaline-earth metals (Be, Mg, Ca) substitution of BFe2XH hydride perovskites for applications as hydrogen storage materials: A DFT perspective, *Int. J. Hydrogen Energy*, 2024, **79**, 1191–1200.

5 A. Kumari, A. Ali, J. A. Abraham, A. K. Mishra, M. Kallel, W. M. Shewakh, S. Formanova and R. Sharma, A Comprehensive DFT Analysis of Novel Vacancy-Ordered Double Perovskites Na2SnX6 (X= Br, I) for the Opto-electronic and Thermoelectric Properties Applications, *J. Inorg. Organomet. Polym. Mater.*, 2025, 1–13.

6 B. P. Finkenauer, Y. Zhang, K. Ma, J. W. Turnley, J. Schulz, M. Gómez, A. H. Coffey, D. Sun, J. Sun and R. Agrawal, Amine-Thiol/Selenol Chemistry for Efficient and Stable Perovskite Solar Cells, *J. Phys. Chem. C*, 2023, **127**(2), 930–938.

7 Best Research-Cell Efficiency Chart, 2025, https://www.nrel.gov/pv/cell-efficiency.html.

8 M. Alla, S. Bimli, V. Manjunath, E. Choudhary, S. Sharma, G. R. Wakale, A. Miglani, M. Rouchdi and B. Fares, Examining the potential of non-toxic stable double perovskite solar cells based on Cs2CuSbX6, *Mater. Today Commun.*, 2023, **36**, 106608.

9 P. P. Boix, S. Agarwala, T. M. Koh, N. Mathews and S. G. Mhaisalkar, Perovskite solar cells: beyond methylammonium lead iodide, *J. Phys. Chem. Lett.*, 2015, **6**(5), 898–907.

10 S. A. Dar and B. S. Sengar, Breakthrough in sustainable photovoltaics: Achieving 30.86% efficiency with innovative lead-free bilayer perovskite solar cells using SCAPS-1D and DFT framework, *Sol. Energy Mater. Sol. Cells*, 2025, **282**, 113352.

11 B. K. Bareth and M. N. Tripathi, High photovoltaic performance of an emerging lead-free chalcogenide perovskite BaHfS3 under high pressure, *Sol. Energy Mater. Sol. Cells*, 2025, **282**, 113445.

12 Y.-Y. Sun, M. L. Agiorgousis, P. Zhang and S. Zhang, Chalcogenide perovskites for photovoltaics, *Nano Lett.*, 2015, **15**(1), 581–585.

13 S. Karthick, S. Velumani and J. Bouclé, Chalcogenide BaZrS3 perovskite solar cells: A numerical simulation and analysis using SCAPS-1D, *Opt. Mater.*, 2022, **126**, 112250.

14 D. C. Hayes, S. Agarwal, K. C. Vincent, I. M. Aimiuwu, A. A. Pradhan, M. C. Uible, S. C. Bart and R. Agrawal, A reliable, colloidal synthesis method of the orthorhombic chalcogenide perovskite, BaZrS 3, and related ABS 3 nanomaterials (A= Sr, Ba; B= Ti, Zr, Hf): a step forward for earth-abundant, functional materials, *Chem. Sci.*, 2025, **16**(3), 1308–1320.

15 N. A. Moroz, C. Bauer, L. Williams, A. Olvera, J. Casamento, A. A. Page, T. P. Bailey, A. Weiland, S. S. Stoyko and E. Kioupakis, Insights on the synthesis, crystal and electronic structures, and optical and thermoelectric properties of Sr1–x Sb x HfSe3 orthorhombic perovskite, *Inorg. Chem.*, 2018, **57**(12), 7402–7411.

16 R. O. Balogun, M. A. Olopade, O. O. Oyebola and A. D. Adewoyin, First-principle calculations to investigate structural, electronic and optical properties of MgHfS3, *Mater. Sci. Eng., B*, 2021, **273**, 115405.

17 H. R. Abdul Ameer, A. N. Jarad, K. H. Salem, H. S. Hadi, M. A. Alkhafaji, R. S. Zabibah, K. A. Mohammed, K. Kumar Saxena, D. Buddhi and H. Singh, A role of back contact and temperature on the parameters of CdTe solar cell, *Adv. Mater. Process. Technol.*, 2024, **10**(2), 497–505.

18 N. Chawki, M. Rouchdi, M. Alla and B. Fares, Numerical modeling of a novel solar cell system consisting of electron Transport material (ETM)/CaZrS3-based chalcogenide perovskites using SCAPS-1D software, *Sol. Energy*, 2024, **274**, 112592.

19 D. Srinivasan, A.-D. Rasu Chettiar, E. N. Vincent Mercy and L. Marasamy, Scrutinizing the untapped potential of emerging ABSe3 (A= Ca, Ba; B= Zr, Hf) chalcogenide perovskites solar cells, *Sci. Rep.*, 2025, **15**(1), 3454.

20 M. K. Hossain, M. H. K. Rubel, G. I. Toki, I. Alam, M. F. Rahman and H. Bencherif, Effect of various electron and hole transport layers on the performance of CsPbI3-based perovskite solar cells: a numerical investigation in DFT, SCAPS-1D, and wxAMPS frameworks, *ACS Omega*, 2022, **7**(47), 43210–43230.

21 H. El-assib, M. Alla, S. Tourougui, M. Alla, F. Elfatouaki, S. A. Dar, A. Chauhan, N. Chawki, N. Shrivastav and V. Manjunath, High-performance optimization and analysis of $Cs_2CuSbCl_6$-Based lead-free double perovskite solar cells with theoretical efficiency exceeding 27%, *Renew. Energy*, 2025, **239**, 122092.

22 B. K. Ravidas, M. K. Roy and D. P. Samajdar, Investigation of photovoltaic performance of lead-free CsSnI3-based perovskite solar cell with different hole transport layers: First Principle Calculations and SCAPS-1D Analysis, *Sol. Energy*, 2023, **249**, 163–173.

23 M. S. Uddin, M. K. Hossain, M. B. Uddin, G. F. Toki, M. Ouladsmane, M. H. Rubel, D. I. Tishkevich, P. Sasikumar, R. Haldhar and R. Pandey, An in-depth investigation of the combined optoelectronic and photovoltaic properties of lead-free Cs2AgBiBr6 double perovskite solar cells using DFT and SCAPS-1D frameworks, *Adv. Electron. Mater.*, 2024, **10**(5), 2300751.

24 S. T. Jan and M. Noman, Comprehensive analysis of heterojunction compatibility of various perovskite solar cells with promising charge transport materials, *Sci. Rep.*, 2023, **13**(1), 19015.

25 K. Deepthi Jayan, Design and Comparative Performance Analysis of High-Efficiency Lead-Based and Lead-Free Perovskite Solar Cells, *Phys. Status Solidi*, 2022, **219**(7), 2100606.

26 J. Liang, Y. Wang, X. Liu, J. Chen, L. Peng and J. Lin, Theoretical analysis of doping of perovskite light-absorbing layer for highly efficient perovskite solar cells, *J. Phys. Chem. Solids*, 2024, **188**, 111901.

27 X. Cai, T. Hu, H. Hou, P. Zhu, R. Liu, J. Peng, W. Luo and H. Yu, A review for nickel oxide hole transport layer and its application in halide perovskite solar cells, *Mater. Today Sustain.*, 2023, **23**, 100438.

28 G. Pindolia, S. M. Shinde and P. K. Jha, Optimization of an inorganic lead free RbGeI3 based perovskite solar cell by SCAPS-1D simulation, *Sol. Energy*, 2022, **236**, 802–821.

29 N. Chawki, M. Rouchdi, M. Alla and B. Fares, Simulation and analysis of high-performance hole transport material SrZrS3-based perovskite solar cells with a theoretical efficiency approaching 26%, *Sol. Energy*, 2023, **262**, 111913.

30 N. Thakur, P. Kumar and P. Sharma, Simulation study of chalcogenide perovskite (BaZrSe3) solar cell by SCAPS-1D, *Mater. Today: Proc.*, 2023, DOI: **10.1016/j.matpr.2023.01.012**.

31 A. Morales-Acevedo, Fundamentals of solar cell physics revisited: Common pitfalls when reporting calculated and measured photocurrent density, open-circuit voltage, and efficiency of solar cells, *Sol. Energy*, 2023, **262**, 111774.